

Contents lists available at ScienceDirect

International Journal of Solids and Structures

journal homepage: www.elsevier.com/locate/ijsolstr





Finite element implementation of a gradient-damage theory for fracture in elastomeric materials

Jaehee Lee a, Seunghyeon Lee a, Shawn A. Chester b, Hansohl Cho a,*

- ^a Department of Aerospace Engineering, Korea Advanced Institute of Science and Technology, Daejeon, 34141, Republic of Korea
- ^b Department of Mechanical Engineering, New Jersey Institute of Technology, Newark, NJ 07102, USA

ARTICLE INFO

Keywords: Gradient-damage theory Elastomer Fracture Finite element

ABSTRACT

We present a finite element implementation procedure for a phase-field framework for fracture in elastomeric materials based on the gradient-damage theory. Governing equations of macroscopic and microscopic force balances, and constitutive theories for large elastic deformation and damage are summarized, and the computational implementation is described in significant detail. To facilitate the computational implementation of the gradient-damage theory for elastomeric materials in a widely available finite element program, the source codes are provided as online Supplemental Materials to this paper. Furthermore, we provide a comparative study of the gradient-damage models with two distinct driving forces for damage: (1) entropy-driven and (2) internal energy-driven. We then show that the internal energy-driven damage model presents more realistic descriptions of the failure that accompanies extreme stretching and scission in elastomeric networks.

1. Introduction

Elastomeric materials are attractive for diverse engineering and biological applications due to their outstanding, reversible extensibility. Hence, there has been increasing demand for a better understanding of deformation and failure events in elastomeric materials subjected to extreme environments. However, predicting and modeling of extreme deformation and failure events in elastomeric materials beyond their reversible deformation limits are very challenging owing to the complexity of the underlying physical mechanisms for irreversible damage processes across multiple length scales.

Over the past two decades, the phase-field approach has gained great attention for modeling damage and failure events in a broad variety of synthetic and natural materials based on variational principles for fracture processes at a continuum level (Francfort and Marigo, 1998; Bourdin et al., 2000; Miehe et al., 2010a,b). By making use of a scalar variable, the phase field, denoted as d (damage) and its gradient, ∇d , the phase-field method has been found to regularize the sharp crack topology by representing a diffusive damage zone within a characteristic length scale (I), by which not only has it overcome numerical difficulties involving sharp crack topologies and discontinuities but has also enabled to simulate mesh-independent crack propagation processes. In addition to the phase-field framework based upon the variational approach, the nonlocal, gradient-type, damage theories have

been formulated to regularize the strain softening due to damage evolution in brittle materials (Pijaudier-Cabot and Bažant, 1987; Peerlings et al., 1996, 1998; de Borst et al., 1999; de Borst, 2002). A variational formulation was also developed in order to overcome the numerical issues involving regularization techniques in the gradient-type, damage theories (Lorentz and Andrieux, 1999; Lorentz and Godard, 2011). More comprehensive reviews on the recent phase-field and nonlocal, gradient theories of fracture in brittle materials can be found in de Borst and Verhoosel (2016). In the meantime, based on these early studies, Miehe and coworkers extended the phase-field approaches to model brittle fracture in finitely stretchable hyperelastic materials (Miehe and Schänzel, 2014; Raina and Miehe, 2016; Gültekin et al., 2016). The seminal work by Miehe and Schänzel has become popular in modeling large deformation and failure events in elastomeric materials over the past several years (Wu et al., 2016; Kumar et al., 2018; Russ et al., 2020).

More recently, more realistic physical pictures of failure in elastomeric networks have been studied by Creton (2017), Long et al. (2021), Chen et al. (2017), and Mao et al. (2017), motivated by the classical work by Lake and Thomas (1967) that recognized that rupture in an elastomeric network is an energetic process dominated by a change in the internal energy due to stretching and scission in molecular bonds. Mao et al. (2017) incorporated the microscopic molecular picture of bond-stretching into the eight-chain network model

E-mail address: hansohl@kaist.ac.kr (H. Cho).

^{*} Corresponding author.

of Arruda and Boyce (1993). Then, these authors proposed a new gradient-damage theory with entropic- and energetic thermodynamic considerations (Talamini et al., 2018; Mao and Anand, 2018a,b) which were not pursued in the variational principle-based phase-field fracture theory in the work of Miehe and coworkers. In their work, the eightchain network model was modified to account for bond-stretching. Furthermore, the macroscopic and microscopic force balances were derived within the virtual-power methods of Frémond and Nedjar (1996) and Gurtin (1996), and new constitutive equations for the gradientdamage framework were introduced. The major point of departure of the framework by Anand and coworkers is that while the previous phase-field fracture theories have been formulated via the variational approach, their gradient-damage theory has been formulated using the principle of virtual power and rigorous thermodynamic considerations. It should also be noted that while the driving force for damage is "entropic" in the earlier hyperelasticity-based failure models by Miehe and coworkers, it is solely "energetic" in the new damage model by Anand and coworkers. Furthermore, in the work of Miehe and coworkers, the gradient-damage term is implied to be dissipative but, in the theory of Anand and coworkers, the origin of the gradient-damage term is clearly energetic in nature.

The phase-field framework combined with the entropy- or internal energy-driven damage models has now found broad success in simulating progressive damage and failure in a variety of elastomeric networks. However, detailed numerical procedures and associated codes for the gradient-damage theory for elastomeric materials are seldom published in the literature. In Molnár and Gravouil (2017) and Kristensen and Martínez-Pañeda (2020), finite element implementation procedures for linear elasticity-based phase field framework have been presented, where they provided user-element (UEL) subroutines in a commercially available program, Abaqus/Standard for handling the damage degree of freedom. In Russ et al. (2020) and Mandal et al. (2020), finite element procedures for the hyperelasticity-based phase field framework have been presented, where these authors did not provide any source codes. More recently, an open-source program, FEniCS (Alnæs et al., 2015) has been amenable for the implementation of the hyperelasticity-based phase field framework in the recent papers by Kumar et al. (2020) and Li and Bouklas (2020), where the Unified Form Language (UFL) (Alnæs et al., 2014) was utilized to compute the complicated tangent moduli for the constitutive models and, accordingly, the computational implementation details were not provided. The main purpose of this paper is therefore to discuss the numerical details of the finite element implementation of the gradient-damage theory for failure in elastomeric materials, following recent studies of the numerical implementations of coupled, multi-physics problems in soft materials (Chester et al., 2015; Henann et al., 2013; Henann and Kamrin, 2016). We have implemented the finite element procedures for the gradient-damage theory by writing user-defined element (UEL) subroutines in Abaqus/Standard, which has been most widely employed for multi-physics problems coupled with nonlinear elasticity. The Abaqus UEL subroutines and associated input files for all numerical examples presented throughout this paper are also available as online Supplemental Materials to this paper. Accordingly, this work also aims to enable research communities working on extreme mechanical behaviors in elastomeric materials to utilize the new gradient-damage framework and associated computational procedures. Furthermore, this work provides a comparative study of gradient-damage theories that employ (1) entropy-driven or (2) internal energy-driven damage models. To this end, we present simulation results of extreme deformation and failure events in synthetic and natural rubbery materials, for which we make use of our numerical implementations for both entropy-driven and internal energy-driven damage models and compare them against experimental data.

The paper is organized as follows. In Section 2, we summarize the gradient-damage theory in which large elastic deformation is coupled with the evolution of a phase-field damage variable. We then

present the finite element implementation of the gradient-damage theory with two distinct driving forces for damage (entropy- and internal energy-driven) in significant detail in Section 3. In Section 4, we show simulation results from examples of various single- and double-notch elastomeric specimens in order to verify our finite element implementations for both damage models. Finally, we apply the numerical capabilities with entropy-driven and internal energy-driven damage models to failure in synthetic and natural rubbery specimens in Section 5. More details of numerical implementation procedures are provided in Appendices A–F.

2. Modeling framework for the gradient-damage theory

In this section, we summarize the gradient-damage theory, in which large elastic deformation is coupled with the evolution of a phase-field damage variable, following Miehe and Schänzel (2014) and Talamini et al. (2018). This theoretical framework of large mechanical deformation coupled with other scalar fields has been extensively employed in many multi-physics problems (Chester and Anand, 2010; Henann et al., 2013; Di Leo et al., 2014; Henann and Kamrin, 2016; Konica and Sain, 2021).

2.1. Summary of the nonlocal continuum model

Kinematics and constitutive equations

A motion ϕ is defined as a one-to-one mapping $x=\phi(X,t)$ with a material point X in a fixed undeformed reference and x in a deformed spatial configuration with deformation gradient $F\stackrel{\text{def}}{=}\frac{\partial \phi}{\partial X}.$ Then, we define the following:

right Cauchy–Green tensor
$$\mathbf{C} = \mathbf{F}^{\top} \mathbf{F}$$

left Cauchy–Green tensor $\mathbf{B} = \mathbf{F} \mathbf{F}^{\top}$
isochoric part of \mathbf{F} $\bar{\mathbf{F}} = J^{-1/3} \mathbf{F}$, $J \stackrel{\text{def}}{=} \det \mathbf{F}$ (1)
isochoric part of \mathbf{C} $\bar{\mathbf{C}} = \bar{\mathbf{F}}^{\top} \bar{\mathbf{F}} = J^{-2/3} \mathbf{C}$
isochoric part of \mathbf{B} $\bar{\mathbf{B}} = \bar{\mathbf{F}} \bar{\mathbf{F}}^{\top} = J^{-2/3} \mathbf{B}$.

A scalar damage field $d \in [0,1]$ is introduced. This phase-field variable characterizes an intact state by d=0 and a fully damaged state by d=1. Then, the free energy $\psi_{\rm R}$ in an undeformed reference degraded due to damage evolution has the form of

$$\begin{aligned} \psi_{\mathbf{R}} &= \hat{\psi}_{\mathbf{R}}(\mathbf{F}, d, \nabla d) \\ &= \hat{\psi}_{\mathbf{R}}^{*}(\mathbf{F}, d) + \hat{\psi}_{\mathbf{R}, \text{nonlocal}}(\nabla d), \end{aligned} \tag{2}$$

where $\nabla d=\frac{\partial d}{\partial \mathbf{X}}$ and $\hat{\psi}_{\mathbf{R}}^*$ is the free energy function that will be detailed in Section 2.2. Also, the nonlocal contribution of the free energy is defined by

$$\hat{\psi}_{\text{R,nonlocal}}(\nabla d) = \frac{1}{2} \varepsilon_{\text{R}}^f l^2 |\nabla d|^2$$
(3)

with the chain scission energy per unit reference volume ε_R^f and the characteristic length scale l that characterizes an intrinsic length scale for the damage process. We then define the first Piola stress T_R ,

$$\mathbf{T}_{\mathrm{R}} = 2\mathbf{F} \frac{\partial \hat{\psi}_{\mathrm{R}}}{\partial \mathbf{C}} \tag{4}$$

Furthermore, the microscopic stresses, ω_R and ξ_R , conjugates to d and ∇d (Gurtin, 1996; Talamini et al., 2018) are

$$\begin{split} & \omega_{\rm R} = \frac{\partial \hat{\psi}_{\rm R}^*}{\partial d} + \omega_{\rm R, diss} \\ & \xi_{\rm R} = \frac{\partial \hat{\psi}_{\rm R, nonlocal}}{\partial \nabla d} = \varepsilon_{\rm R}^f l^2 \nabla d \end{split} \tag{5}$$

where the dissipative part of ω_R can be divided into a rate independent part and a rate dependent part as follows: $\omega_{R,diss} = \alpha + \zeta_R \dot{d}$. The rate-independent part α represents the dissipated chain scission energy per unit volume during damage evolution, i.e., $\alpha = \varepsilon_R^f$.

Governing equations and boundary conditions

The governing partial differential equations in the undeformed reference consist of the following:

1. Macroforce balance

$$DivT_{R} + \mathbf{b}_{R} = 0 \tag{6}$$

with the body force \mathbf{b}_{R} in the reference. Here, inertial effects are neglected.

2. Microforce balance

$$Div\xi_{R} - \omega_{R} = 0. \tag{7}$$

Substituting the constitutive equations in Eq. (5) for the microforce balance in Eq. (7), we obtain

$$\zeta_{\rm R}\dot{d} = -\frac{\partial \hat{\psi}_{\rm R}^*}{\partial d} + \varepsilon_{\rm R}^f l^2 \Delta d - \varepsilon_{\rm R}^f \tag{8}$$

where Δ denotes the referential Laplacian; i.e., $\Delta d = \text{Div}(\nabla d)$.

Then, let $S_{\mathbf{\phi}}$ and $S_{\mathbf{t}_R}$ be complementary subsurfaces of the boundary ∂B of the body B, i.e., $\partial B = S_{\mathbf{\phi}} \cup S_{\mathbf{t}_R}$ and $S_{\mathbf{\phi}} \cap S_{\mathbf{t}_R} = \emptyset$. For a time interval $t \in [0,T]$, we consider a set of boundary conditions given by

$$\begin{cases} \boldsymbol{\varphi} = \check{\boldsymbol{\psi}} & \text{on } S_{\boldsymbol{\varphi}}, \\ T_{R} \mathbf{n}_{R} = \check{\boldsymbol{t}}_{R} & \text{on } S_{\boldsymbol{t}_{R}}. \end{cases}$$
 (9)

We also introduce a set of complementary subsurfaces S_d and S_{ξ_R} , i.e., $\partial B = S_d \cup S_{\xi_R}$ and $S_d \cap S_{\xi_R} = \varnothing$. We assume that the gradient of damage is perpendicular to the boundary surface, which implies no damage flux on the surface (Mao and Anand, 2018b; Russ et al., 2020). Thus,

$$\begin{cases} d = 0 & \text{on } S_d, \\ \nabla d \cdot \mathbf{n}_{R} = 0 & \text{on } S_{\xi_{R}}. \end{cases}$$
 (10)

The initial condition is given as $d(\mathbf{X}, 0) = 0$ in \mathcal{B} .

2.2. Entropy- vs. internal energy-driven damage models

In this section, we outline two different damage models which have been widely accepted for modeling the progressive damage and fracture in elastomeric materials over the past decade. Specifically, in the two approaches, a damage process is assumed to be (1) entropy-driven or (2) internal energy-driven. Entropy-driven damage was initially proposed for modeling large deformation brittle fracture in elastomers in Miehe and Schänzel (2014). The degraded free energy function due to damage has the form of

$$\hat{\psi}_{\mathbf{R}}^{*}(\mathbf{F}, d) = g(d)\,\hat{\psi}_{\mathbf{R}}^{0}(\mathbf{F}) \tag{11}$$

where $\hat{\psi}_{R}^{0}$ is the free energy of the undamaged body. The monotonically decreasing degradation function g(d) has the following properties:

$$g'(d) \le 0$$
 with $g(0) = 1$, $g(1) = 0$, and $g'(1) = 0$. (12)

We employ a simple function $g(d)=(1-d)^2$ that satisfies the above properties. Hence, the microforce balance in Eq. (8) can be rewritten as

$$\zeta_{\mathbf{R}}\dot{d} = 2(1-d)\hat{\psi}_{\mathbf{R}}^0 + \varepsilon_{\mathbf{R}}^f l^2 \Delta d - \varepsilon_{\mathbf{R}}^f. \tag{13}$$

To enforce the constraint $d \in [0,1]$ and irreversibility in damage growth $(\dot{d}>0)$, a monotonically increasing history function is introduced (Miehe et al., 2010a; Talamini et al., 2018),¹

$$\mathcal{H}_{R}(t) = \max_{s \in [0,t]} \langle \hat{\psi}_{R}^{0}(\mathbf{F}(s)) - \varepsilon_{R}^{f}/2 \rangle, \tag{14}$$

$$\mathcal{H}_{\mathbf{R}}(t) = \max_{s \in [0,t]} \hat{\psi}_{\mathbf{R}}^{0}(\mathbf{F}(s)),$$

for the examples with the Gaussian entropy-driven model in Fig. 1, 2 and 5.

where $\langle \cdot \rangle$ are Macaulay brackets, i.e., $\langle x \rangle = \begin{cases} 0, & x < 0, \\ x, & x \ge 0. \end{cases}$ Then, the microforce balance in Eq. (13) becomes

$$\zeta_{\mathbf{R}}\dot{d} = 2(1-d)\mathcal{H}_{\mathbf{R}} - \varepsilon_{\mathbf{R}}^{f}(d-l^{2}\Delta d). \tag{15}$$

From the classical rubber elasticity with the Gaussian statistics of a chain network, the undamaged free energy function takes the form of

$$\hat{\psi}_{R}^{0} = \frac{3}{2} \mu (\bar{\lambda}^{2} - 1) + \frac{K}{2} (J - 1)^{2} \quad \text{where} \quad \bar{\lambda} = \sqrt{\frac{1}{3} \text{tr} \bar{C}}, \tag{16}$$

also known as the nearly incompressible neo-Hookean representation. Here, μ is the initial shear modulus (rubbery modulus) and K is the bulk modulus. The degraded Piola stress due to damage growth is then given by

$$\mathbf{T}_{\mathbf{R}} = (1 - d)^{2} \left[\mu \left(\mathbf{J}^{-2/3} \mathbf{F} - \bar{\lambda}^{2} \mathbf{F}^{-\mathsf{T}} \right) + K(J - 1) \mathbf{J} \mathbf{F}^{-\mathsf{T}} \right]. \tag{17}$$

Furthermore, with the non-Gaussian statistics of a chain network, we may employ the nearly incompressible Arruda-Boyce representation by taking the undamaged free energy function of

$$\hat{\psi}_{R}^{0} = Nnk_{b}\theta \left[\left(\frac{\bar{\lambda}}{\sqrt{n}} \right) \beta + \ln \left(\frac{\beta}{\sinh \beta} \right) \right] + \frac{K}{2} (J - 1)^{2} \quad \text{with}$$

$$\beta = \mathcal{L}^{-1} \left(\frac{\bar{\lambda}}{\sqrt{n}} \right)$$
(18)

where N is the number of chains per unit volume, n is the number of Kuhn segments in a chain, k_b is Boltzmann's constant, and \mathcal{L}^{-1} denotes the inverse of the Langevin function $\mathcal{L}(x) = \coth x - x^{-1}$. The degraded Piola stress is then given by

$$\mathbf{T}_{R} = (1 - d)^{2} \left[\bar{\mu} \left(J^{-2/3} \mathbf{F} - \bar{\lambda}^{2} \mathbf{F}^{-\mathsf{T}} \right) + K(J - 1) J \mathbf{F}^{-\mathsf{T}} \right] \quad \text{where}$$

$$\bar{\mu} = \frac{\mu}{3} \frac{\sqrt{n}}{\bar{\lambda}} \mathcal{L}^{-1} \left(\frac{\bar{\lambda}}{\sqrt{n}} \right). \tag{19}$$

It should be noted that in these models in which the driving force for damage is either the Gaussian or non-Gaussian entropic change, as the damage variable, d, grows, both the deviatoric and volumetric parts of the Piola stress degrade. The Gaussian entropic elasticity-based damage model in Eqs. (16) and (17) has been extensively employed for modeling of failure in synthetic elastomers and biological tissues (Raina and Miehe, 2016; Kumar et al., 2018; Russ et al., 2020) over the last decade given that it is relatively straightforward to implement and computationally efficient for use in finite element solvers. However, the Gaussian or non-Gaussian entropy-driven damage is not physically consistent with the argument by Lake and Thomas (1967). According to their work, rupture is an energetic process resulting from bond-stretching and scission in a polymer network upon deformation; this has been well recognized and accepted in the polymer physics and mechanics communities over the past five decades.

Recently, the argument by Lake and Thomas (1967) has been extended to describe the energetic process during rupture in an elastomeric network (Mao et al., 2017; Talamini et al., 2018; Mao and Anand, 2018b,a). In their papers, the model significantly departs from Miehe and Schänzel's work, especially with regard to the driving force for damage. They argued that the evolution of a damage field should be driven by the internal energy change due to bond-stretching and scission, reflecting the original idea by Lake and Thomas (1967). Hence, they introduced the effective bond stretch $\lambda_b = L_t/L_0$, where L_0 is the initial Kuhn segment length and L_t is the current Kuhn segment length, which is central to their new model. Upon a bond stretch, the degraded free energy function has the form of

$$\hat{\psi}_{R}^{*}(\mathbf{F}, \lambda_{b}, d) = g(d)\,\hat{\varepsilon}_{R}^{0}(\mathbf{F}, \lambda_{b}) - \vartheta\,\hat{\eta}_{R}(\mathbf{F}, \lambda_{b}) \tag{20}$$

where $\hat{\epsilon}_{\rm R}^0$ is the internal energy of the undamaged body and $\hat{\eta}_{\rm R}$ is the configurational entropy of the chain network. Employing the same

¹ We have used a history function defined in Miehe et al. (2010a), Miehe and Schänzel (2014) as.

degradation function $g(d) = (1 - d)^2$, the microforce balance in Eq. (8) is rewritten as

$$\zeta_{\mathbf{R}}\dot{d} = 2(1-d)\mathcal{H}_{\mathbf{R}} - \varepsilon_{\mathbf{p}}^{f}(d-l^{2}\Delta d) \tag{21}$$

where the history function is defined by

$$\mathcal{H}_{\mathbf{R}}(t) = \max_{s \in [0,t]} \langle \hat{\varepsilon}_{\mathbf{R}}^{0}(\mathbf{F}(s), \lambda_{b}(s)) - \varepsilon_{\mathbf{R}}^{f}/2 \rangle. \tag{22}$$

Furthermore, the undamaged internal energy is defined by

$$\hat{\varepsilon}_{R}^{0} = \frac{1}{2} N n E_{b} \left(\lambda_{b} - 1 \right)^{2} + \frac{K}{2} (J - 1)^{2}$$
(23)

where E_b is the bond-stiffness related to the stretching of Kuhn segments. Furthermore, as in the Arruda-Boyce model, the configurational entropy of the chain network is expressed as

$$\hat{\eta}_{R} = -Nnk_{b} \left[\left(\frac{\bar{\lambda}\lambda_{b}^{-1}}{\sqrt{n}} \right) \beta + \ln \left(\frac{\beta}{\sinh \beta} \right) \right] \quad \text{with} \quad \beta = \mathcal{L}^{-1} \left(\frac{\bar{\lambda}\lambda_{b}^{-1}}{\sqrt{n}} \right). \tag{24}$$

The degraded free energy function is hence expressed as

$$\begin{split} \hat{\psi}_{\mathrm{R}}^* &= (1 - d)^2 \hat{\varepsilon}_{\mathrm{R}}^0 - \theta \hat{\eta}_{\mathrm{R}} \\ &= (1 - d)^2 \left[\frac{1}{2} N n E_b \left(\lambda_b - 1 \right)^2 + \frac{K}{2} (J - 1)^2 \right] \\ &+ N n k_b \theta \left[\left(\frac{\bar{\lambda} \lambda_b^{-1}}{\sqrt{n}} \right) \beta + \ln \left(\frac{\beta}{\sinh \beta} \right) \right]. \end{split} \tag{25}$$

Here, it should be noted that, as the damage grows, only the internal energy degrades. Moreover, as is well discussed in Mao et al. (2017), $\bar{\lambda}\lambda_b^{-1}$ can be interpreted as the effective chain stretch due to Kuhn segment rearrangement that goes toward the intrinsic chain extensibility, $\lambda_L = \sqrt{n}$. Then, the degraded Piola stress in the modified Arruda-Boyce representation with bond-stretching can be expressed by

$$\mathbf{T}_{R} = \bar{\mu} \left(J^{-2/3} \mathbf{F} - \bar{\lambda}^{2} \mathbf{F}^{-T} \right) + (1 - d)^{2} K (J - 1) J \mathbf{F}^{-T} \quad \text{where}$$

$$\bar{\mu} = \frac{\mu}{3} \frac{\sqrt{n}}{\bar{\lambda} \lambda_{b}} \mathcal{L}^{-1} \left(\frac{\bar{\lambda} \lambda_{b}^{-1}}{\sqrt{n}} \right). \tag{26}$$

Furthermore, from the thermodynamic argument posited in Talamini et al. (2018), the bond stretch, λ_b , is determined by solving the following implicit equation,

$$(1-d)^2 E_b(\lambda_b - 1) - k_b \vartheta\left(\frac{\bar{\lambda}}{\sqrt{n}\lambda_b^2}\right) \mathcal{L}^{-1}\left(\frac{\bar{\lambda}\lambda_b^{-1}}{\sqrt{n}}\right) = 0.$$
 (27)

This implicit equation is derived from another microscopic force balance in which the bond stretch indeed minimizes the free energy, i.e., $\frac{\partial \hat{\psi}_R}{\partial \lambda_h} = 0$.

These constitutive models in Eqs. (11)–(27) complete the formulation of boundary value problems on displacement and damage fields together with the governing partial differential equations in Eqs. (6)–(10).

3. Finite element implementation

In this section, we present detailed numerical procedures for the gradient-damage theory described in Section 2. We have implemented the coupled gradient-damage theory by writing user-defined element (UEL) subroutines in Abaqus/Standard. The source codes for the UEL subroutines are provided together with input files as an online supplement to this paper.

3.1. Discretization of weak forms

Neglecting body forces, the strong form for the boundary value problem of coupled momentum and damage fields consists of the following:

$$\begin{cases} \boldsymbol{\phi} = \check{\boldsymbol{\phi}} & \text{on} \quad S_{\boldsymbol{\phi}}, \\ \mathbf{T}_R \mathbf{n}_R = \check{\mathbf{t}}_R & \text{on} \quad S_{\mathbf{t}_R}, \end{cases}$$
 (28) Balance of microforce for damage
$$\begin{cases} \zeta_R \dot{d} = 2(1-d)\mathcal{H}_R & \\ -\varepsilon_R^f (d-l^2 \Delta d) & \text{in} \quad \mathcal{B}_R, \\ d = 0 & \text{on} \quad S_d, \\ \nabla d \cdot \mathbf{n}_R = 0 & \text{on} \quad S_{\xi_R}. \end{cases}$$

The boundary value problem is then rewritten in the following weak form with two weighting fields \mathbf{w}_1 and \mathbf{w}_2 which vanish on S_u and S_d , respectively.

$$\begin{cases}
\int_{\mathcal{B}_{R}} \left(\mathbf{T}_{R} : \frac{\partial \mathbf{w}_{1}}{\partial \mathbf{X}} \right) dv_{R} = \int_{\mathcal{S}_{\mathbf{t}_{R}}} \left(\mathbf{w}_{1} \cdot \check{\mathbf{t}}_{R} \right) da_{R}, \\
\int_{\mathcal{B}_{R}} \left[\mathbf{w}_{2} \left(\zeta_{R} \dot{d} - 2(1 - d) \mathcal{H}_{R} + \varepsilon_{R}^{f} d \right) + \varepsilon_{R}^{f} l^{2} \left(\frac{\partial \mathbf{w}_{2}}{\partial \mathbf{X}} \cdot \frac{\partial d}{\partial \mathbf{X}} \right) \right] dv_{R} = 0.
\end{cases}$$
The body is approximated by finite elements. The trial solutions for

The body is approximated by finite elements. The trial solutions for the displacement and damage fields are interpolated by the nodal displacements \mathbf{u}^A and the nodal damage d^A via the shape functions N^A with the index $A=1,2,\ldots$ denoting the nodes of the element,

$$\mathbf{u} = \sum \mathbf{u}^A N^A \quad \text{and} \quad d = \sum d^A N^A. \tag{30}$$

In addition, following a standard Galerkin procedure, the weighting (or test) fields are interpolated by the same shape functions,

$$\mathbf{w}_1 = \sum \mathbf{w}_1^A N^A \quad \text{and} \quad \mathbf{w}_2 = \sum \mathbf{w}_2^A N^A. \tag{31}$$

Plugging Eqs. (30) and (31) into (29), we obtain the following element-level equations for each of the finite elements \mathcal{B}_{p}^{e} ,

$$\int_{\mathcal{B}_{R}^{e}} \left(\mathbf{T}_{R} \frac{\partial N^{A}}{\partial \mathbf{X}} \right) dv_{R} = \int_{\mathcal{S}_{t_{R}}^{e}} \left(N^{A} \check{\mathbf{t}}_{R} \right) da_{R},$$

$$\int_{\mathcal{B}_{R}^{e}} \left[N^{A} \left(\zeta_{R} \dot{d} - 2(1 - d) \mathcal{H}_{R} + \varepsilon_{R}^{f} d \right) + \varepsilon_{R}^{f} l^{2} \left(\frac{\partial N^{A}}{\partial \mathbf{X}} \cdot \frac{\partial d}{\partial \mathbf{X}} \right) \right] dv_{R} = 0.$$
(32)

The discretized, element-level equations are solved by a Newton-type iteration procedure, which requires residuals and tangents. First, we define the following element-level residuals for the displacement and damage fields. Using index notation, the residuals are expressed as

$$\begin{cases} \left(R_{u_i}\right)^A = -\int_{B_{\mathbb{R}}^c} \left(T_{\mathbb{R}}\right)_{ij} \frac{\partial N^A}{\partial X_j} dv_{\mathbb{R}} + \int_{S_{\mathbb{I}_{\mathbb{R}}}^c} \left(N^A \check{\mathbf{I}}_{\mathbb{R},i}\right) da_{\mathbb{R}}, \\ \left(R_d\right)^A = -\int_{B_{\mathbb{R}}^c} \left[N^A \left(\zeta_{\mathbb{R}} \dot{d} - 2(1-d)\mathcal{H}_{\mathbb{R}} + \varepsilon_{\mathbb{R}}^f d\right) + \varepsilon_{\mathbb{R}}^f l^2 \left(\frac{\partial N^A}{\partial X_j} \frac{\partial d}{\partial X_j}\right)\right] dv_{\mathbb{R}}. \end{cases}$$

$$(33)$$

Furthermore, tangents for the iterative Newton solution procedure are obtained as

$$\mathbf{K}_{\mathbf{u}\mathbf{u}}^{AB} = -\frac{\partial \mathbf{R}_{\mathbf{u}}^{A}}{\partial \mathbf{u}^{B}}, \quad \mathbf{K}_{\mathbf{u}d}^{AB} = -\frac{\partial \mathbf{R}_{\mathbf{u}}^{A}}{\partial d^{B}},$$

$$\mathbf{K}_{d\mathbf{u}}^{AB} = -\frac{\partial R_{d}^{A}}{\partial \mathbf{u}^{B}}, \quad K_{dd}^{AB} = -\frac{\partial R_{d}^{A}}{\partial d^{B}}.$$
(34)

Using index notation, we have the following tangents $\mathbf{K}_{\mathbf{n}\mathbf{n}}^{AB}$ and K_{dd}^{AB} ,

$$\begin{cases} K_{u_{l}u_{k}}^{AB} = \int_{B_{R}^{c}} \frac{\partial N^{A}}{\partial X_{j}} \left(\frac{\partial T_{R,ij}}{\partial F_{kl}} \right) \frac{\partial N^{B}}{\partial X_{l}} dv_{R} - \int_{S_{t_{R}}^{c}} N^{A} N^{B} \frac{\partial \check{T}_{R,i}}{\partial u_{k}} da_{R}, \\ K_{dd}^{AB} = \int_{B_{R}^{c}} \left[N^{A} \left(\zeta_{R} \frac{\partial \dot{d}}{\partial d} + 2\mathcal{H}_{R} + \varepsilon_{R}^{f} \right) N^{B} + \frac{\partial N^{A}}{\partial X_{j}} \left(\varepsilon_{R}^{f} l^{2} \right) \frac{\partial N^{B}}{\partial X_{j}} \right] dv_{R} \end{cases}$$
(35)

where $\frac{\partial \dot{d}}{\partial d} = \frac{1}{\Delta t}$ with a time step of Δt . The tangent modulus $\frac{\partial T_{R,ij}}{\partial F_{kl}}$ central to the linearization process in the nonlinear finite element procedures for both damaged or undamaged hyperelastic materials is detailed in

Section 3.3. Specifically, the tangent moduli for damaged neo-Hookean as well as damaged Arruda-Boyce representations with bond-stretching are discussed in significant detail.

Furthermore, we provide the corresponding finite-element procedures for the gradient-damage theory in the spatial configuration for completeness. From the principles of virtual power, the governing partial differential equations in the deformed spatial configuration are given as shown below.

1. Macroforce balance

$$\operatorname{div}\mathbf{T} + \mathbf{b} = \mathbf{0} \tag{36}$$

with the Cauchy stress $\mathbf{T} = J^{-1}\mathbf{T}_{\mathbf{R}}\mathbf{F}^{\top}$ and body force \mathbf{b} in the deformed configuration.

2. Microforce balance

$$\operatorname{div}\xi - \omega = 0 \tag{37}$$

where the microscopic stresses, ω and ξ , conjugates to d and grad d, are defined by

$$\omega = J^{-1} \frac{\partial \hat{\psi}_{R}}{\partial d} + \varepsilon^{f} + \zeta \dot{d},$$

$$\xi = J^{-1} \frac{\partial \hat{\psi}_{R}}{\partial \operatorname{grad} d},$$
(38)

i.e., $\omega=J^{-1}\omega_{\rm R}$ and $\xi=J^{-1}{\rm F}\xi_{\rm R}$ with the chain scission energy per unit volume $\varepsilon^f=J^{-1}\varepsilon_{\rm R}^f$ and the kinetic modulus $\zeta=J^{-1}\zeta_{\rm R}$, where $J={\rm det}{\rm F}$ is the volume change. Then, the microforce balance in Eq. (37) can be rewritten as

$$\zeta \dot{d} - 2(1 - d)\mathcal{H} + \varepsilon^f d - \operatorname{div} \xi = 0. \tag{39}$$

where the spatial history function $\mathcal{H} = J^{-1}\mathcal{H}_{R}$ according to the definition in Eq. (14).

The strong form expressed in the deformed body B is then given by,

Balance of momentum
$$\begin{cases} \mathbf{u} = \check{\mathbf{u}} & \text{on } S_{\mathbf{u}}, \\ \mathbf{Tn} = \check{\mathbf{t}} & \text{on } S_{\mathbf{t}}, \end{cases}$$
Balance of microforce for damage
$$\begin{cases} \zeta \dot{d} - 2(1 - d)\mathcal{H} \\ + \varepsilon^f d - \operatorname{div} \xi = 0 & \text{in } B, \\ d = 0 & \text{on } S_d, \end{cases}$$

$$\begin{cases} d = 0 & \text{on } S_d, \\ d = 0 & \text{on } S_d, \end{cases}$$

The boundary value problem is then rewritten in the following weak form with two weighting fields \mathbf{w}_1 and \mathbf{w}_2 which vanish on S_u and S_d , respectively:

$$\begin{cases}
\int_{B} \left(\mathbf{T} : \frac{\partial \mathbf{w}_{1}}{\partial \mathbf{x}} \right) dv = \int_{S_{\mathbf{t}}} \left(\mathbf{w}_{1} \cdot \check{\mathbf{t}} \right) da, \\
\int_{B} \left[\mathbf{w}_{2} \left(\zeta \dot{d} - 2(1 - d)\mathcal{H} + \varepsilon^{f} d \right) + \frac{\partial \mathbf{w}_{2}}{\partial \mathbf{x}} \cdot \xi \right] dv = 0.
\end{cases} \tag{41}$$

Then, the spatial forms of the residuals are expressed as

$$\begin{cases} \left(R_{u_i}\right)^A = -\int_{\mathcal{B}^e} T_{ij} \frac{\partial N^A}{\partial x_j} dv + \int_{S_{\mathbf{t}}^e} \left(N^A \check{t}_i\right) da, \\ \left(R_d\right)^A = -\int_{\mathcal{B}^e} \left[N^A \left(\zeta d - 2(1-d)\mathcal{H} + \varepsilon^f d\right) + \varepsilon^f l^2 F_{mj} F_{nj} \left(\frac{\partial N^A}{\partial x_m} \frac{\partial d}{\partial x_n}\right)\right] dv, \end{cases}$$

$$(42)$$

where $\xi_m=J^{-1}\frac{\partial \hat{\psi}_{\rm R}}{\partial ({\rm grad}\,d)_m}=\varepsilon^f l^2 F_{mj}F_{nj}\frac{\partial d}{\partial x_n}$ was used. Finally, the corresponding tangents in the spatial configuration are given by

$$\begin{cases} K_{u_{l}u_{k}}^{AB} = \int_{B^{e}} \frac{\partial N^{A}}{\partial x_{j}} \left(\mathbb{A}_{ijkl} \right) \frac{\partial N^{B}}{\partial x_{l}} dv - \int_{S_{\mathbf{t}}^{e}} N^{A} N^{B} \frac{\partial \check{\mathbf{t}}_{i}}{\partial u_{k}} da, \\ K_{dd}^{AB} = \int_{B^{e}} \left[N^{A} \left(\zeta \frac{\partial \dot{d}}{\partial d} + 2\mathcal{H} + \varepsilon^{f} \right) N^{B} + \frac{\partial N^{A}}{\partial x_{m}} \left(\varepsilon^{f} l^{2} F_{mj} F_{nj} \right) \frac{\partial N^{B}}{\partial x_{n}} \right] dv, \end{cases}$$

$$(43)$$

where the spatial tangent modulus, $\mathbb{A}_{ijkl} = F_{ln} \frac{\partial T_{ij}}{\partial F_{kn}} = J^{-1} F_{jm} F_{ln} \frac{\partial T_{R,im}}{\partial F_{kn}}$. The referential and spatial tangent moduli are further discussed in Section 3.3.

We have implemented both of the referential and spatial finite element formulations and confirmed that these two formulations gave exactly the same residuals and tangents. For brevity, we will focus on numerical procedures in the referential formulation for the rest of this paper. Moreover, we have developed four-noded isoparametric quadrilateral plane-strain and plane-stress elements as well as an eight-noded three-dimensional element. Especially for the plane-strain and the 3D elements, we have utilized the *F-bar* method (de Souza Neto et al., 1996) in order to avoid locking-related issues. Details of the procedure for implementing the *F-bar* method are provided in Appendix B. Furthermore, a detailed solution procedure for the plane-stress condition (imposing zero-stress conditions at the element level) is discussed in Section 3.4.

3.2. Numerical solution procedure

In this section, we outline numerical solution procedures of the coupled deformation-phase-field equations. The overall framework for the solution procedure is also summarized in Box 1.

Firstly, we summarize state variables in the numerical solution procedure, i.e.,

- Given as initial guesses: $\{\mathbf{u}_{n+1}, d_{n+1}\}$ at time t_{n+1}
- Known: $\{\mathbf{F}_n, d_n, \mathcal{H}_{R,n}\}$ at time t_n
- Calculate: $\{\mathbf{T}_{\mathbf{R},\mathbf{n}+1},\mathcal{H}_{\mathbf{R},n+1},\mathbf{R}_{\mathbf{u}},R_d,\mathbf{K}_{\mathbf{u}\mathbf{u}},K_{dd}\}$ at time t_{n+1}

To decouple the deformation-phase-field equations in our solution procedure, first we determine the current history function $\mathcal{H}_{R,n+1}$ using the previous deformation gradient \mathbf{F}_n at time t_n (Miehe et al., 2010a), i.e.,

$$\mathcal{H}_{R,n+1}(\mathbf{F}_n) = \begin{cases} \langle \hat{\psi}_R^0(\mathbf{F}_n) - \varepsilon_R^f/2 \rangle & \text{for } \langle \hat{\psi}_R^0(\mathbf{F}_n) - \varepsilon_R^f/2 \rangle > \mathcal{H}_{R,n} \\ \mathcal{H}_{R,n} & \text{otherwise} \end{cases}$$
(44)

for the entropy-driven damage model, and

$$\mathcal{H}_{R,n+1}(\mathbf{F}_n) = \begin{cases} \langle \hat{\varepsilon}_{R}^{0}(\mathbf{F}(s), \lambda_b(s)) - \varepsilon_{R}^{f}/2 \rangle & \text{for } \langle \hat{\varepsilon}_{R}^{0}(\mathbf{F}_n, \lambda_{b,n}) - \varepsilon_{R}^{f}/2 \rangle > \mathcal{H}_{R,n} \\ \mathcal{H}_{R,n} & \text{otherwise} \end{cases}$$
(45)

for the internal energy-driven damage model. In contrast, for fully coupled, monolithic solution procedures, this is computed using the current deformation gradient \mathbf{F}_{n+1} in the governing equation for the damage field (Miehe et al., 2010b; Reinoso et al., 2017). Then, the residuals are computed by

$$\begin{pmatrix} R_{u_i} \end{pmatrix}^A = -\int_{B_R^e} \left(\mathbf{T}_R(\mathbf{F}_{n+1}, d_{n+1}) \right)_{ij} \frac{\partial N^A}{\partial X_j} dv_R + \int_{S_{\mathbf{f}_R}^e} \left(N^A \check{\mathbf{t}}_{R,i} \right) da_R,
\begin{pmatrix} R_d \end{pmatrix}^A = -\int_{B_R^e} \left[N^A \left(\zeta_R \dot{d} - 2(1 - d_{n+1}) \mathcal{H}_{R,n+1}(\mathbf{F}_n) + \varepsilon_R^f d_{n+1} \right) \right.
\left. + \varepsilon_R^f l^2 \left(\frac{\partial N^A}{\partial X_i} \frac{\partial d}{\partial X_i} \right) \right] dv_R.$$
(46)

It should be noted that the displacement and damage fields are calculated simultaneously at each time increment in Abaqus/Standard. However, the equation systems are weakly decoupled by the current history function computed via \mathbf{F}_n . In our solution procedure, we made use of an analysis step *COUPLED TEMPERATURE-DISPLACEMENT provided in Abaqus/Standard by which the damage field is treated as the scalar temperature field. We then solved (1) the momentum equation and (2) the damage equation separately using an iterative Newton method by declaring *SOLUTION TECHNIQUE, TYPE=SEPARATED in the Abaqus input files. This solution procedure we have employed slightly underestimates the rate of the damage evolution compared to fully coupled solution procedures. However, we have confirmed that

the simulation results using our solution procedure are nearly identical to those with the fully coupled procedure when the time increment is sufficiently small.

Remark. Our solution procedure implemented in Abaqus/Standard is slightly different from the original "staggered" scheme for this coupled deformation-phase-field theory presented by Miehe and coworkers (Miehe et al., 2010a; Hofacker and Miehe, 2012; Miehe and Schänzel, 2014; Miehe et al., 2015). In their papers, the phase-field d_{n+1} is calculated by solving the minimization problem of the crack topology using the previous displacement field \mathbf{u}_n , i.e.,

$$\begin{aligned} d_{n+1} &= \arg\inf_{d} \left\{ \int_{\mathcal{B}_{\mathbf{R}}} \left[\zeta (d_{n+1} - d_{n})^{2} - (1 - d_{n+1})^{2} \,\mathcal{H}(\mathbf{u}_{n}) \right. \right. \\ &\left. + \varepsilon_{\mathbf{R}}^{f} \left(\frac{1}{2} d_{n+1}^{2} + \frac{l^{2}}{2} |\nabla d|^{2} \right) \right] dv \right\}. \end{aligned}$$

The displacement field \mathbf{u}^{n+1} is then calculated using the current d^{n+1} obtained from the previous linear problem,

$$\mathbf{u}_{n+1} = \arg\inf_{\mathbf{u}} \left\{ \int_{B_{\mathbf{R}}} \left[\psi_{\mathbf{R}}(\mathbf{F}_{n+1}, d_{n+1}) - \mathbf{b} \cdot \mathbf{u}_{n+1} \right] dv \right\}.$$

Box 1. Numerical solution procedure

- 1. Initialize the displacement $\mathbf{u}_{n+1}^{(0)}$ and damage field $d_{n+1}^{(0)}$ at time t_{n+1} obtained from extrapolation. The variables $\{\mathbf{F}_n,d_n,\mathcal{H}_{\mathbf{R},n}\}$ at time t_n are also given
 - 2. Compute the history function $\mathcal{H}_{R,n+1}^{(i)}$
 - 3. Calculate the first Piola stress $\mathbf{T}_{R,n+1}^{(i)}$, tangent modulus $\left(\partial \mathbf{T}_R/\partial \mathbf{F}\right)_{n+1}^{(i)}$, and internal variables
 - 4. Calculate the residuals $\mathbf{R}_{\mathbf{u}}$, R_d and tangents $\mathbf{K}_{\mathbf{u}\mathbf{u}}$, K_{dd}
 - 5. Check the residuals $|\mathbf{R}_{\mathbf{u}}|, |R_d| < tolerance \rightarrow Go$ to 8
 - 6. Update $\mathbf{u}_{n+1}^{(i+1)} = \mathbf{u}_{n+1}^{(i)} + \Delta \mathbf{u}$ and $d_{n+1}^{(i+1)} = d_{n+1}^{(i)} + \Delta d$
 - 7. $i = i + 1 \to \text{Go to } 2$
- 8. Update the displacement \mathbf{u}_{n+1} and damage field d_{n+1} at time t_{n+1}

3.3. Updating stress, tangent and internal variables

Here, we include the details of computing stresses, tangent moduli and internal variables for both entropy- and internal energy-driven damage models.

3.3.1. Entropy-driven damage model: Gaussian and non-gaussian entropic elasticity

The first Piola stress for the nearly incompressible neo-Hookean representation at time t_{n+1} is

$$\mathbf{T}_{\mathbf{R},n+1} = \left[(1 - d_{n+1})^2 + k \right] \left[\mu \left(J_{n+1}^{-2/3} \mathbf{F}_{n+1} - \bar{\lambda}_{n+1}^2 \mathbf{F}_{n+1}^{-\mathsf{T}} \right) + K(J_{n+1} - 1) J_{n+1} \mathbf{F}_{n+1}^{-\mathsf{T}} \right]. \tag{47}$$

It should be noted that the degradation function is modified as $g(d) = (1-d)^2 + k$ with $k \approx 10^{-4}$ in order to avoid computational difficulty when the damage field d approaches 1. Moreover, the referential tangent modulus $\frac{\partial T_R}{\partial F}$ is expressed as

$$\frac{\partial (T_{R})_{ij}}{\partial F_{kl}} = \left[(1 - d)^{2} + k \right]
\left[\mu \left\{ J^{-2/3} \delta_{ik} \delta_{jl} - \frac{2}{3} J^{-2/3} F_{kl}^{-\top} F_{ij} - 2\bar{\lambda} \frac{\partial \bar{\lambda}}{\partial F_{kl}} F_{ij}^{-\top} + \bar{\lambda}^{2} F_{li}^{-1} F_{jk}^{-1} \right\}
+ K \left\{ (2J - 1)J F_{kl}^{-\top} F_{ij}^{-\top} - (J - 1)J F_{li}^{-1} F_{jk}^{-1} \right\} \right]$$
(48)

using the identities

$$\left(\frac{\partial \mathbf{F}}{\partial \mathbf{F}}\right)_{ijkl} = \delta_{ik}\delta_{jl}, \quad \left(\frac{\partial \mathbf{F}^{-\mathsf{T}}}{\partial \mathbf{F}}\right)_{ijkl} = -F_{li}^{-1}F_{jk}^{-1}, \quad \text{and} \quad \left(\frac{\partial J}{\partial \mathbf{F}}\right)_{kl} = JF_{kl}^{-\mathsf{T}},$$

$$(49)$$

and

$$\left(\frac{\partial \bar{\lambda}}{\partial \mathbf{F}}\right)_{kl} = \frac{1}{3\bar{\lambda}} \left(J^{-2/3} F_{kl} - \bar{\lambda}^2 F_{kl}^{-\mathsf{T}}\right). \tag{50}$$

Furthermore, the first Piola stress for the nearly incompressible Arruda-Boyce representation at time t_{n+1} is

$$\mathbf{T}_{\mathbf{R},n+1} = \left[(1 - d_{n+1})^2 + k \right] \left[\bar{\mu} \left(J_{n+1}^{-2/3} \mathbf{F}_{n+1} - \bar{\lambda}_{n+1}^2 \mathbf{F}_{n+1}^{-\mathsf{T}} \right) + K(J_{n+1} - 1) J_{n+1} \mathbf{F}_{n+1}^{-\mathsf{T}} \right]$$
(51)

where $\bar{\mu} = \frac{\mu}{3} \frac{\sqrt{n}}{\bar{\lambda}_{n+1}} \mathcal{L}^{-1} \left(\frac{\bar{\lambda}_{n+1}}{\sqrt{n}} \right)$. Moreover, the referential tangent modulus $\frac{\partial T_R}{\partial F}$ is expressed as

$$\frac{\partial \left(T_{R}\right)_{ij}}{\partial F_{kl}} = \left[(1-d)^{2} + k \right] \\
\times \left[\bar{\mu} \left(J^{-2/3} \delta_{ik} \delta_{jl} - \frac{2}{3} J^{-2/3} F_{kl}^{-\mathsf{T}} F_{ij} - 2\bar{\lambda} \frac{\partial \bar{\lambda}}{\partial F_{kl}} F_{ij}^{-\mathsf{T}} + \bar{\lambda}^{2} F_{li}^{-1} F_{jk}^{-1} \right) \\
+ \frac{\partial \bar{\mu}}{\partial F_{kl}} \left(J^{-2/3} F_{ij} - \bar{\lambda}^{2} F_{ij}^{-\mathsf{T}} \right) \\
+ K \left\{ (2J-1)J F_{kl}^{-\mathsf{T}} F_{ij}^{-\mathsf{T}} - (J-1)J F_{li}^{-1} F_{jk}^{-1} \right\} \right]$$
(52)

where

$$\frac{\partial \bar{\mu}}{\partial F_{kl}} = -\bar{\mu}\bar{\lambda}^{-1} \left(1 - \frac{r}{\beta} \frac{\partial \beta}{\partial r} \right) \quad \text{with} \quad r = \frac{\bar{\lambda}}{\sqrt{n}} \quad \text{and} \quad \beta = \mathcal{L}^{-1}(r). \tag{53}$$

3.3.2. Internal energy-driven damage model

The bond stretch λ_b is computed by solving the following implicit equation at each integration point,

$$\begin{split} & \left[(1 - d_{n+1})^2 + k \right] E_b(\lambda_{b,n+1} - 1) \\ & - k_b \vartheta \left(\frac{\bar{\lambda}_{n+1}}{\sqrt{n} \left(\lambda_{b,n+1} \right)^2} \right) \mathcal{L}^{-1} \left(\frac{\bar{\lambda}_{n+1} \left(\lambda_{b,n+1} \right)^{-1}}{\sqrt{n}} \right) = 0. \end{split} \tag{54}$$

As the damage variable d approaches 1, finding the bond stretch is very difficult since it grows extremely rapidly together with the damage variable; the implicit equation becomes extremely stiff near $d \rightarrow 1$. In order to resolve this numerical issue, we have employed the rtsafe algorithm, for which a Newton iteration is combined with a bisection method, as detailed in Press et al. (2007).

Remark. An approximate solution for the bond stretch λ_b was provided in Li and Bouklas (2020) by approximating the inverse Langevin function as $\mathcal{L}^{-1} \approx \frac{1}{\mathrm{sign}(x)-x}$ if $0.84136 \leq |x| < 1$ to avoid the iterative procedure at the Gauss point level.

The first Piola stress for the nearly incompressible modified Arruda-Boyce model with bond-stretching is

$$\mathbf{T}_{\mathbf{R},n+1} = \bar{\mu} \left(J_{n+1}^{-2/3} \mathbf{F}_{n+1} - \bar{\lambda}_{n+1}^2 \mathbf{F}_{n+1}^{-\top} \right) + \left[(1 - d_{n+1})^2 + k \right] K(J_{n+1} - 1) J_{n+1} \mathbf{F}_{n+1}^{-\top}$$
(55)

where $\bar{\mu} = \frac{\mu}{3} \frac{\sqrt{n}}{\bar{\lambda}_{n+1} \lambda_{b,n+1}} \mathcal{L}^{-1} \left(\frac{\bar{\lambda}_{n+1}}{\lambda_{b,n+1} \sqrt{n}} \right)$. Then, the referential tangent modulus, $\frac{\partial \mathbf{T}_R}{\partial \mathbf{F}}$ is

$$\frac{\partial \left(T_{R}\right)_{ij}}{\partial F_{kl}}\bigg|_{d} = \frac{\partial \left(T_{R}\right)_{ij}}{\partial F_{kl}}\bigg|_{\lambda_{b},d} + \frac{\partial \left(T_{R}\right)_{ij}}{\partial \lambda_{b}}\bigg|_{\mathbf{E},d} \frac{\partial \lambda_{b}}{\partial F_{kl}}\bigg|_{d}. \tag{56}$$

The first term $\frac{\partial (T_{\rm R})_{ij}}{\partial F_{kl}}$ is identical to Eq. (52) by replacing $r=\frac{\bar{\lambda}\lambda_b^{-1}}{\sqrt{n}}$. Then, the second term is expressed as

$$\frac{\partial \left(T_{R}\right)_{ij}}{\partial \lambda_{b}}\bigg|_{F,d} = \frac{\partial \bar{\mu}}{\partial \lambda_{b}} \left(J^{-2/3}F_{ij} - \bar{\lambda}^{2}F_{ij}^{-\mathsf{T}}\right) \quad \text{where} \quad \frac{\partial \bar{\mu}}{\partial \lambda_{b}} = -\bar{\mu}\bar{\lambda}_{b}^{-1} \left(1 + \frac{r}{\beta} \frac{\partial \beta}{\partial r}\right)$$
(57)

$$\left. \frac{\partial \lambda_b}{\partial F_{kl}} \right|_d = -B^{-1} A_{kl}. \tag{58}$$

Finally, we obtain $A_{kl} dF_{kl} + B d\lambda_b + C dd = 0$ by taking derivatives on the implicit equation for the bond stretch λ_h from Eq. (54). Then,

$$\begin{split} A_{kl} &= -\left(\beta + r\frac{\partial\beta}{\partial r}\right)\frac{\partial r}{\partial\bar{\lambda}}\frac{\partial\bar{\lambda}}{\partial F_{kl}},\\ B &= \left[(1-d)^2 + k\right]\frac{E_b}{k_b\theta}(2\lambda_b - 1) - \left(\beta + r\frac{\partial\beta}{\partial r}\right)\frac{\partial r}{\partial\lambda_b},\\ C &= -2(1-d)\frac{E_b}{k_b\theta}(\lambda_b - 1)\lambda_b. \end{split} \tag{59}$$

For verification of the analytical tangent modulus, we compared simulation results of some deformation experiments against those with a numerical tangent modulus in Appendix C.

3.4. Imposing a plane-stress condition

Here, we outline a simple procedure for imposing a plane-stress condition, i.e., $T_{R_{n+1}}(3,3) = 0$. In the two-dimensional analysis involving both plane-strain and plane-stress situations, the components of a stress tensor and a deformation gradient should be reduced to in-plane components, i.e., $\mathbf{T}_{R}^{*} = (T_{R,11}, T_{R,21}, T_{R,12}, T_{R,22})^{\mathsf{T}}$ and $\mathbf{F}^{*} =$ $(F_{11}, F_{21}, F_{12}, F_{22})^{\mathsf{T}}$, respectively. Specifically, the algorithms described in Klinkel and Govindjee (2002) are employed to enforce the planestress condition, $T_{R,n+1}(3,3) = 0$, by which the unknown out-of-plane component $F_{n+1}(3,3)$ is determined. The algorithm for determining the unknown $F_{n+1}(3,3)$ is summarized in Algorithm 1.

Algorithm 1 Plane-stress algorithm

- 1: Initialize $F_{n+1}^0(3,3) = F_n(3,3)$

 - 2: Calculate stress $\mathbf{T}_{\mathbf{R},n+1}^{i}\left(\mathbf{F}_{n+1}^{i}\right)$ and tangent $\partial \mathbf{T}_{\mathbf{R},n+1}^{i}/\partial \mathbf{F}_{n+1}^{i}$ 3: Check stress $|T_{\mathbf{R},n+1}^{i}(3,3)| < tolerance \to \mathbf{Go}$ to 6 4: Update $F_{n+1}^{i+1}(3,3) = F_{n+1}^{i}(3,3) + \Delta F_{n+1}^{i}$ where ΔF_{n+1}^{i} $-\frac{\partial T_{R,n+1}^{i} / \partial F_{n+1}^{i}(3,3,3,3)}{5: i = i + 1 \rightarrow \text{Go to } 2}$
- 6: Update the deformation gradient $F_{n+1}(3,3) = F_{n+1}^{i}(3,3)$

After the solution procedure for the unknown $F_{n+1}(3,3)$, the referential tangent modulus required in the global Newton iteration procedure is replaced for the plane-stress situation via the static condensation, as

$$\begin{bmatrix} dT_{R,11} \\ dT_{R,21} \\ dT_{R,12} \\ dT_{R,22} \\ dT_{R,33} \end{bmatrix} = \begin{bmatrix} A_{11} & A_{12} \\ A_{21} & A_{22} \end{bmatrix} \begin{bmatrix} dF_{11} \\ dF_{21} \\ dF_{12} \\ dF_{22} \\ dF_{33} \end{bmatrix}.$$
 (60)

Let $d\mathbf{T}_{\mathbf{R}}^* = (dT_{\mathbf{R},11},\,dT_{\mathbf{R},21},\,dT_{\mathbf{R},12},\,dT_{\mathbf{R},22})^{\mathsf{T}}$ and $d\mathbf{F}^* = (dF_{11},\,dF_{21},\,dF_{12},\,dF_{12},\,dF_{22})^{\mathsf{T}}$. Since $dT_{\mathbf{R},33} = 0$, we have

$$d\mathbf{F}_{33} = -\mathbb{A}_{22}^{-1} \mathbb{A}_{21} d\mathbf{F}^*. \tag{61}$$

The plane-stress tangent modulus is then obtained by

$$d\mathbf{T}_{R}^{*} = \mathbb{A}_{ps} d\mathbf{F}^{*}$$
 where $\mathbb{A}_{ps} = \mathbb{A}_{11} - \mathbb{A}_{12} \mathbb{A}_{22}^{-1} \mathbb{A}_{21}$. (62)

The plane-stress algorithm for the internal energy-driven (Arruda-Boyce with no bond-stretching) model is verified through the deformation-only problems in Appendix D, in which we compare results of inhomogeneous deformation fields in notched specimens under Mode-I tension from our UEL implementation against corresponding results obtained from the built-in material models and the plane-stress elements provided in Abagus/Standard.

4. Verification of implementation

In this section, we verify our numerical implementation of the gradient-damage theory with two driving forces for damage by simulating several important benchmark problems in various settings given in Miehe and Schänzel (2014) and Talamini et al. (2018). Specifically, we consider the following examples:

- · Penny-shaped specimen in a plane strain condition
- · Single-edge-notched specimen in a plane stress condition
- · Double-edge-notched specimen in both plane strain and plane stress conditions

4.1. Penny-shaped specimen in tension

First, we have simulated the fracture response of a penny-shaped specimen precracked in its center under plane-strain tension, as illustrated in Miehe and Schänzel (2014). Here, the Gaussian entropy-driven damage model with a compressible neo-Hookean representation was employed.² Fig. 1 displays the simulation results with three different mesh densities with $h = 0.5 \times 10^{-3}$, 1×10^{-3} , and 2×10^{-3} mm near the crack propagation zone. The material parameters used in this set of simulations are given in Table 1.

As shown in Fig. 1(a) and (b), the overall responses in the forcedisplacement curves in our numerical simulations match those in Miehe and Schänzel (2014) well. Furthermore, the simulation results converged with the finest mesh density. However, crack propagation in our simulations was found to be slightly faster than that in Miehe and Schänzel (2014). This discrepancy presumably stems from the difference in the solution procedures used in our work and in Miehe and Schänzel (2014). As described in Section 3.2, we updated the displacement \mathbf{u}_{n+1} and the damage d_{n+1} simultaneously for each time increment while the history function \mathcal{H}_{n+1} was computed with the previous displacement \mathbf{u}_n . However, in their original staggered scheme, the damage d_{n+1} was initially determined from the microforce balance using the previous displacement \mathbf{u}_n . The displacement field \mathbf{u}_{n+1} was then updated in Miehe and Schänzel (2014). Further, Fig. 2 shows the sequential, deformed configurations of the penny-shaped specimen displayed together with the damage contour. Elements with an average value of d > 0.95 are removed in the plots. The damage field began to develop near the initial crack. Then, as nicely depicted in our numerical simulations, the crack propagated throughout the specimen until the specimen finally separated into two parts.

Table 1 Material parameters used in penny-shaped specimens in plane-stress tension.

μ [MPa]	ν	$\varepsilon_{\mathrm{R}}^{f}$ [MPa]	l [mm]	ζ [MPa s]
5	0.45	240	0.01	0.001

4.2. Flaw-sensitivity in single-edge-notched specimen

Next, we present our simulation results for single-edge-notched specimens in plane-stress Mode-I loading illustrated in Talamini et al.

² The free energy function is expressed as $\hat{\psi}_0(\mathbf{F}) = \frac{\mu}{2} [\text{tr}(\mathbf{F}\mathbf{F}^{\mathsf{T}}) - 3] +$ $\frac{\mu}{R}[(\det \mathbf{F})^{-\beta} - 1]$, where $\beta = 2\nu/1 - 2\nu$ with the Poisson's ratio $\nu = 0.45$.

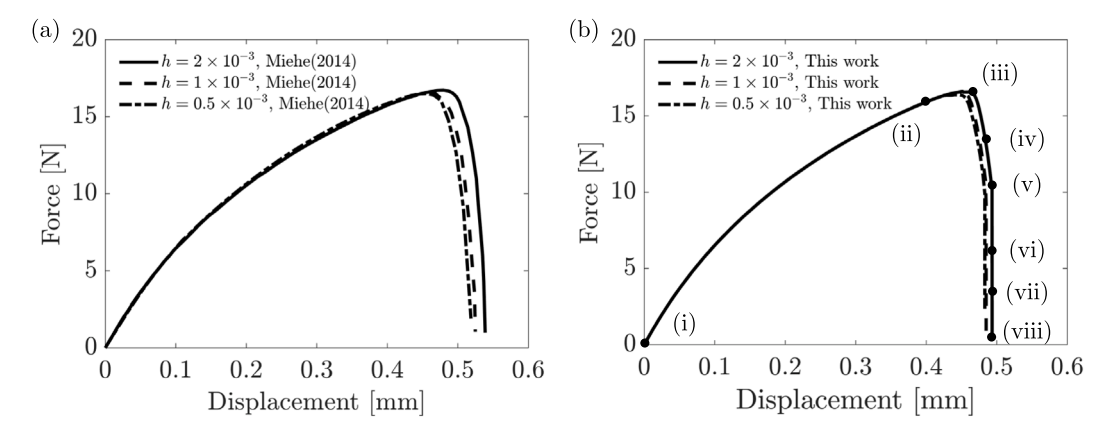


Fig. 1. Force vs. displacement curves in a penny-shaped specimen in plane-strain tension with different mesh sizes of $h = 0.5 \times 10^{-3}$, 1×10^{-3} , and 2×10^{-3} mm (a) in Miehe and Schänzel (2014) and (b) in this work.

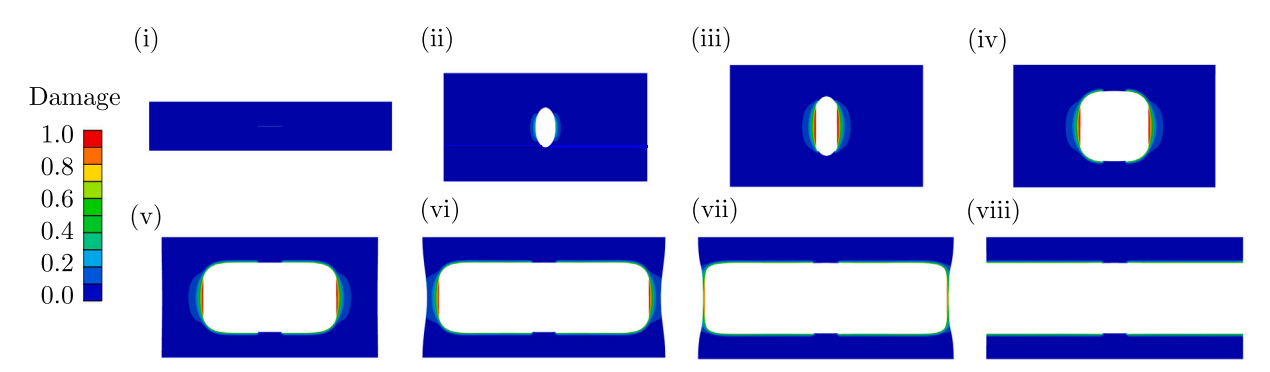


Fig. 2. Deformed configurations of the penny-shaped specimen plotted together with contours of the damage field. Elements are removed from the plots when the damage d > 0.95. (See Video S1 in the Supplemental Material).

(2018), where they considered a series of single-edge-notched specimens with geometrical similarities for the notch lengths $a = \{0.5, 1, 5, 10\} \mu m$, the specimen width was W = 10a and the specimen height was H = 40a. Moreover, a fixed notch-root radius $R = 1 \mu m$ was given for all cases. The material parameters used in our simulations are given in Table 2. In Fig. 3, the normal stressstretch curves with different notch lengths of $a/l = \{0.5, 1, 5, 10\}$ are given (the characteristic length $l=1~\mu m$ is fixed). Here, the internal energy-driven damage evolution model was employed together with a modified Arruda-Boyce representation with the bond stretch described in Section 2.2.3 Our simulation results nicely matched those presented in Talamini et al. (2018). Furthermore, interestingly, as the notch length (or the specimen size) decreased, the rupture stretch significantly increased due to the nonlocal characteristic in the gradient-damage theory; i.e., the size-dependent fracture behavior in this highly stretchable elastomeric materials (strained up to ~ 300%) is reasonably described in the gradient-damage theory.

Fig. 4 shows the deformed specimen together with the damage variable, d, from our simulation. Our simulation reproduced very well the detailed fracture process from the blunted notch (ii), damage initiation (iii), and progressive rupturing (iv, v) to the final failed configuration. More interestingly, with the internal energy-driven damage model (modified Arruda-Boyce with bond-stretching), the simulation results clearly show substantially stiffened behavior just before fracture (or the sudden drop in the stress–stretch curves), as evidenced in all specimen sizes displayed in Fig. 3.

Table 2Material parameters used in the single-edge-notched specimens.

μ [MPa]	K [MPa]	N	$\bar{E}_b = NnE_b$ [MPa]	$\varepsilon_{\mathrm{R}}^{f}$ [MPa]	<i>l</i> [μm]	ζ [MPa s]
0.25	625	4	500	50	1	50

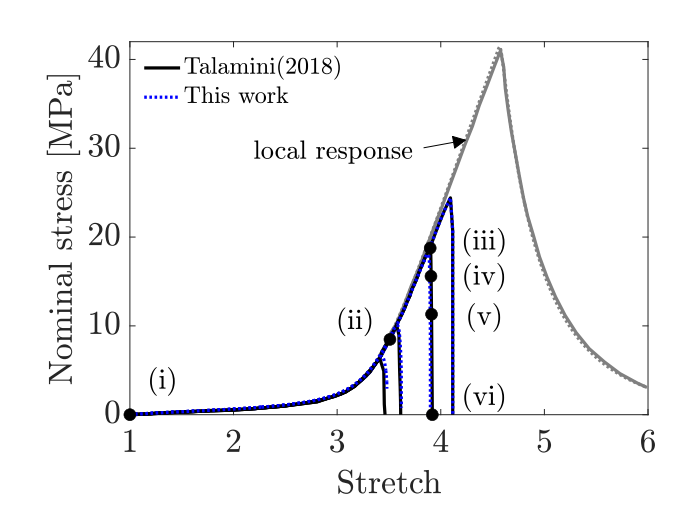


Fig. 3. Nominal stress vs. stretch curves of single-edge-notched specimens in plane-stress tension with $a/l = \{0.5, 1, 5, 10\}$ in Talamini et al. (2018) (black solid lines) and this work (blue dashed lines); Gray lines: local response in a homogeneous deformation state without notch.

³ We used the *Stabilize option in Abaqus to stabilize the solution procedure when the damage was fully developed. See the input files for detail.

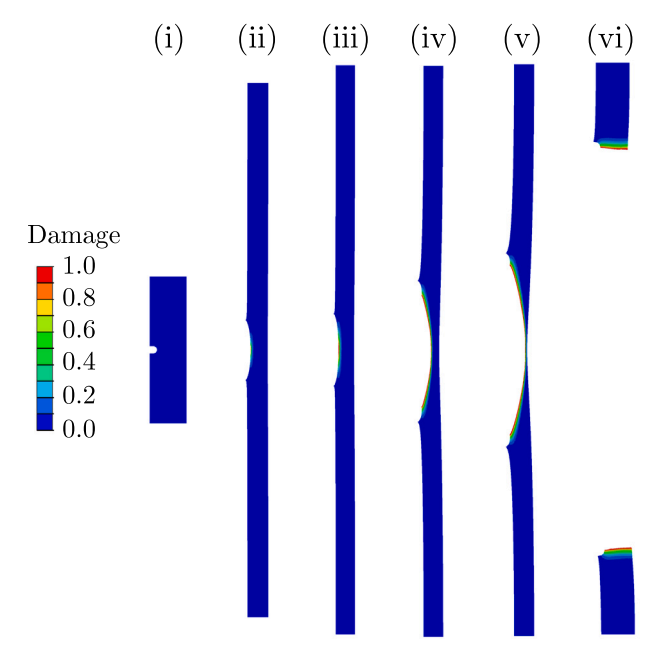


Fig. 4. Progressive damage in deformed configurations of a single-edge-notched specimen for the case of a/l=1. Elements with d>0.95 are removed from the plots. (See Video S2 in the Supplemental Material).

4.3. Double-edge-notched specimen in tension

As a last benchmark problem, we consider double-edge-notched specimens under Model-I tensile loading as illustrated both in Miehe and Schänzel (2014) and Talamini et al. (2018). In their papers, the fracture in a styrene butadiene elastomer (Hocine et al., 2002) was reproduced in numerical simulations under a plane strain condition (Miehe and Schänzel, 2014) and under a plane stress condition (Talamini et al., 2018). Here, we numerically simulate fracture in double-edge-notched specimens with a wide range of notch lengths.

Figs. 5 and 6 show our numerical simulation results of a series of double-edge-notched specimens with various notch lengths of $a=\{12,16,20,24,28\}$ mm under plane-strain tension and plane-stress tension, respectively. The specimen size was fixed at 80 mm (width) \times 200 mm (height) with a specimen depth of 3 mm and a notch-root radius of 0.5 mm. While the Gaussian entropy-driven damage model was used in the plane-strain cases (Fig. 5), the internal energy-driven damage model was used in the plane-stress cases (Fig. 6). Moreover, the material parameters used in these simulations are given in Tables 3 and 4.

As shown in the force displacement curves, our numerical simulations matched very nicely those presented in Miehe and Schänzel (2014) and in Talamini et al. (2018). Furthermore, with both of the entropy- and internal energy-driven mechanisms, it was clearly observed that the initial stiffness as well as the final rupture stretch decreased as the notch length increased. It should also be noted that the overall features during fracture predicted by the Gaussian entropydriven mechanism were found to be very similar to those with the internal energy-driven mechanism. In the internal energy-driven model, the limiting chain extensibility λ_L was taken to be $\lambda_L = \sqrt{1000}$. The large value of the number of effective chain segments, n, in the Arruda-Boyce model approached the neo-Hookean response with no locking behavior, i.e., in all cases presented in Figs. 5 and 6, just before fracture, no marked stiffening behavior was observed. Finally, Fig. 7 shows sequential images of the stretched specimen with the notch length of a = 12 mm under plane-stress tension (Fig. 6). The numerical simulation clearly displays the entire fracture process from crack opening, progressive rupturing to the final failure.

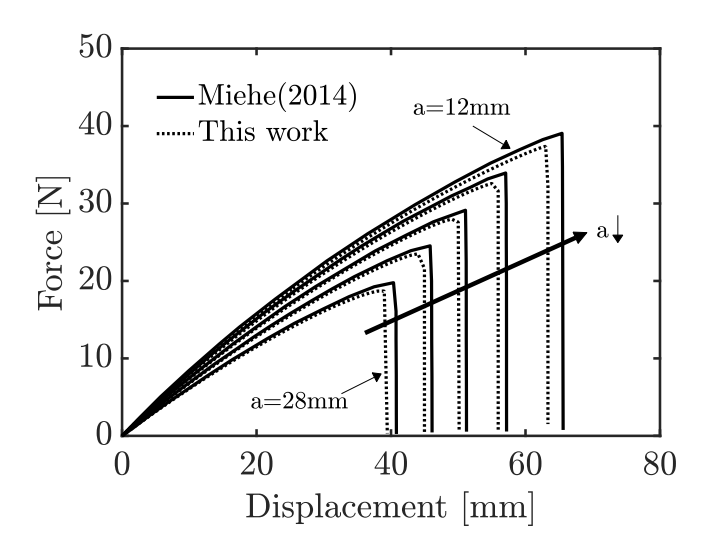


Fig. 5. Force vs. displacement curves of double-edge-notched specimens with increased notch lengths of $a = \{12, 16, 20, 24, 28\}$ mm with the entropy-driven damage model.

Table 3
Material parameters used in the double-edge-notched specimens in Fig. 5.

Parties				-0
μ [MPa]	ν	$\epsilon_{\mathrm{R}}^{f}$ [MPa]	l [mm]	ζ [MPa s]
0.203	0.45	2.67	1	0.001

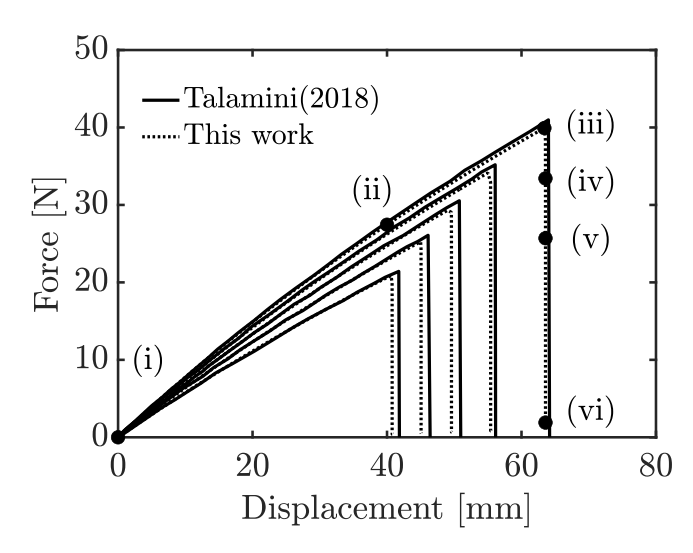


Fig. 6. Force vs. displacement curves of double-edge-notched specimens with increased notch lengths of $a=\{12,16,20,24,28\}$ mm with the internal energy-driven damage model.

Table 4
Material parameters used in the double-edge-notched specimens in Fig. 6.

μ [MPa]	K [MPa]	N	\bar{E}_b [MPa]	ϵ_{R}^f [MPa]	l [mm]	ζ [MPa s]	_
0.268	2.68	1000	15	0.47	1	0.01	-

5. Entropy- and internal energy-driven damage models: A comparative study

This section provides a comparative study of the entropy- and internal energy-driven damage models described in Sections 2 and 3.4 First,

⁴ We have used a history function defined in Eq. (14) throughout all examples for (both Gaussian and non-Gaussian) entropy- or internal energy-driven damage models presented in Section 5.

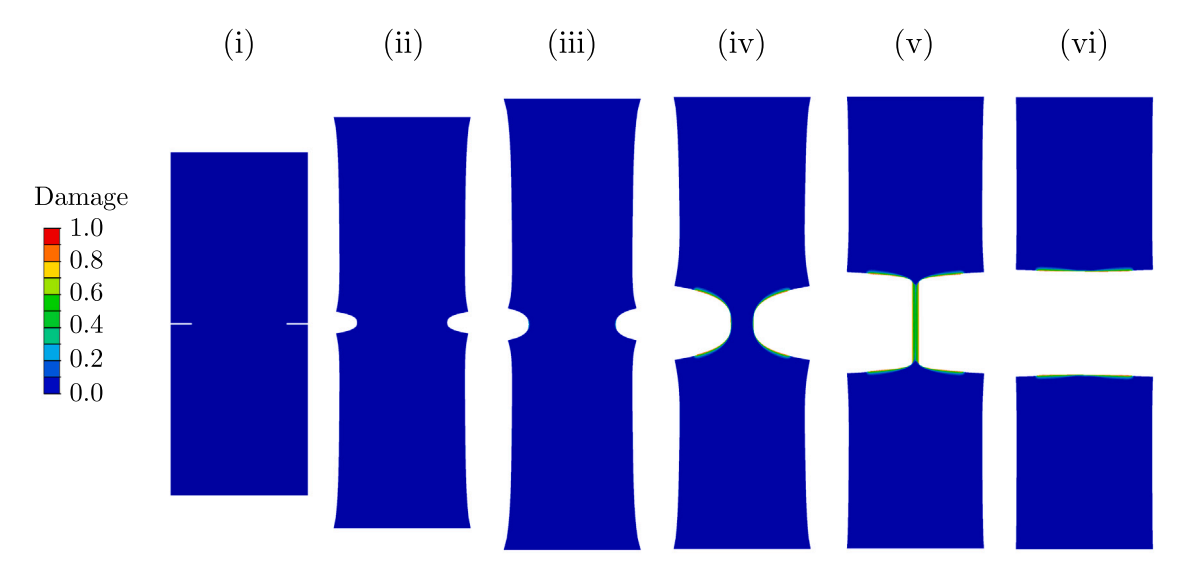


Fig. 7. Progressive damage in deformed configurations of a double-edge-notched specimen for the case of a = 12 mm under plane-stress tension. Elements with d > 0.95 are removed from the plots. (See Video S3 in the Supplemental Material).

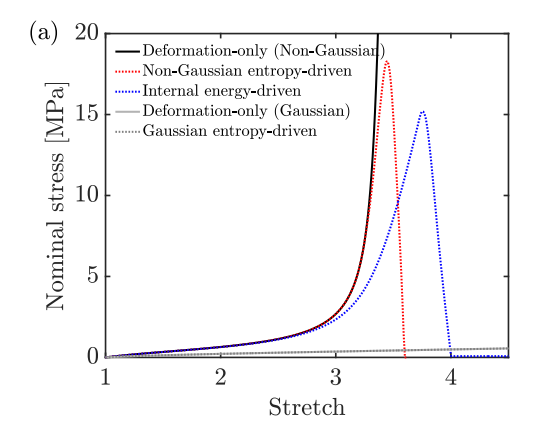
Fig. 8(a) shows the stress-strain curves of local responses of a hyperelastic specimen simulated with (1) Gaussian entropy-driven damage model (neo-Hookean), (2) non-Gaussian entropy-driven damage model (Arruda-Boyce) and (3) internal energy-driven damage model (modified Arruda-Boyce with bond-stretching). All of these local damage responses (dashed lines) are compared against their corresponding deformation-only cases (solid lines) without any damage. The material parameters used in the simulations are listed in Table 5. Furthermore, no initial notch was introduced in the specimen in order to exclude the nonlocal, size-effect. The initial elastic responses are almost identical in all stress-stretch curves from the models with or without damage. As the deformation approaches the limiting chain extensibility $(\sqrt{N} = \sqrt{4})$, both of the non-Gaussian entropy-driven damage model (Arruda-Boyce) and internal energy-driven damage model (modified Arruda-Boyce with bond-stretching) exhibit the significant hardening behavior due to the locking of chain networks. However, in the internal energy-driven damage model, the hardening behavior is observed at a larger stretch since the effective "entropic" stretch, $\bar{\lambda}\lambda_h^{-1}$, grows slower towards the limiting chain extensibility as the "energetic" bond stretch increases before failure. Accordingly, stress degradation due to damage growth is delayed with the same chain scission energy, $\varepsilon_{\rm R}^J$. Furthermore, as expected, the Gaussian entropy-driven damage model never exhibits any hardening behavior, as shown in Fig. 8(b).

Table 5
Material parameters used in simulations of homogeneous deformation with or without damage.

	μ [MPa]	K [MPa]	N	\bar{E}_b [MPa]	$\varepsilon_{\mathrm{R}}^{f}$ [MPa]
Deformation-only (Non-Gaussian)	0.25	625	4	N/A	N/A
Non-Gaussian entropy-driven	0.25	625	4	N/A	6
Internal energy-driven	0.25	625	4	500	6
Deformation-only (Gaussian)	0.25	625	N/A	N/A	N/A
Gaussian entropy-driven	0.25	625	N/A	N/A	6

N/A: Not applicable.

Next, in Fig. 9, we compare the numerically simulated stress-stretch-failure curves with the three different hyperelasticity-based damage theories against experimental data in a synthetic elastomeric material, poly(methyl-acrylate) (PMA) reported in Slootman et al. (2022). In their experiment, it should be noted that final fracture in the PMA elastomer occurs without any dramatic hardening behavior. With the material parameters listed in Table 6, all of the three numerical simulations with (1) Gaussian entropy-driven damage model (neo-Hookean), (2) non-Gaussian entropy-driven damage model (Arruda-Boyce) and (3) internal energy-driven damage model (modified Arruda-Boyce with bond-stretching) nicely capture the overall stress–stretch-failure behavior experimentally observed. First, it is not



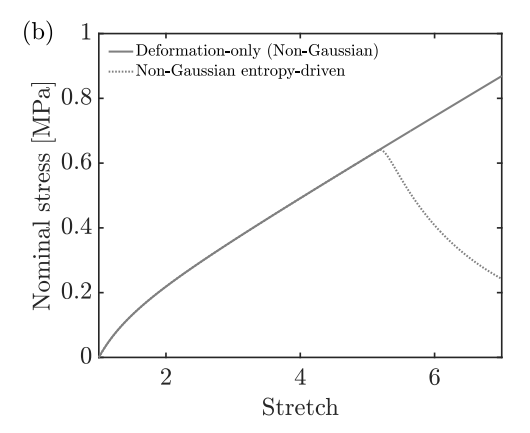


Fig. 8. Comparison of nominal stress-stretch curves in homogeneous local responses with or without damage. Here, the solid lines represent responses without any damage (deformation only) and the dashed lines represent responses with damage evolution.

Table 6
Material parameters used in simulations of a PMA specimen in tension.

	μ [MPa]	K [MPa]	N	\bar{E}_b [MPa]	$\epsilon_{\mathrm{R}}^{f}$ [MPa]	l [mm]	ζ [MPa s]
Non-Gaussian entropy-driven	0.32	300	50	N/A	3.2	0.5	0.01
Internal energy-driven	0.4	300	50	15	0.54	0.5	0.01
Gaussian entropy-driven	0.32	300	N/A	N/A	2.3	0.5	0.01

N/A: Not applicable.

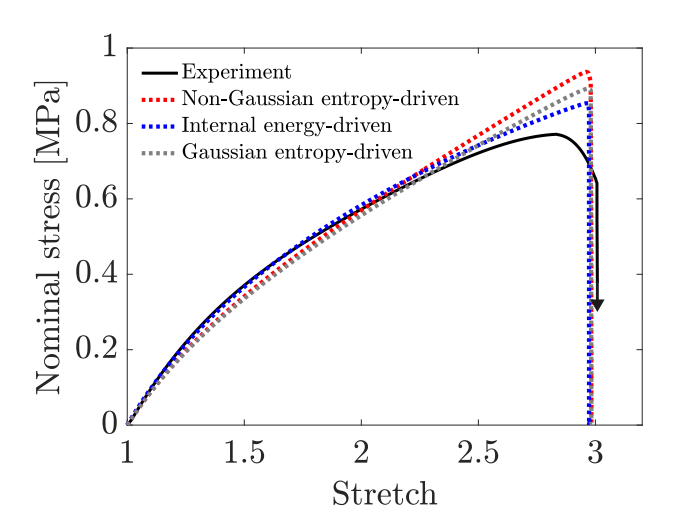


Fig. 9. Nominal stress vs. stretch curves of a PMA specimen in tension. Here, the solid line represents experimental data and the dashed lines represent simulation results with the Gaussian entropy-driven damage model (gray dashed line), non-Gaussian entropy-driven damage model (red dashed line) and internal energy-driven damage model (blue dashed line).

very surprising that there is no significant difference between the responses with the two Gaussian (black dashed line) and non-Gaussian (red dashed line) entropy-driven damage models since the limiting chain extensibility in the Arruda-Boyce representation was taken to be very large. Furthermore, the numerically simulated stress-stretchfailure behavior with the non-Gaussian entropy-driven damage model (red dashed line) is very similar to that with the internal energy-driven damage model (blue dashed line). This supports that, just before the final fracture, the bond-stretch in the modified Arruda-Boyce representation does not evolve significantly. This is quite reasonable since the final fracture in this material occurs at a moderate stretch much smaller than the locking stretch. However, $\varepsilon_{\mathrm{R}}^f$ in the internal energy-driven damage model had to be much smaller than that in the non-Gaussian entropy-driven damage model in order to fit the experimental data.5 This clearly supports that only the internal energy part out of the total free energy contributes "effectively" to failure in the elastomer network in the internal energy-driven damage model with the modified Arruda-Boyce representation with bond-stretching. This example clearly shows that, even when final failure occurs at a moderate stretch much smaller than the locking stretch, the internal energy-driven damage model with the key idea by Lake and Thomas still can provide a more realistic "physical" picture for failure in an elastomer network.

We then examine the simulation capabilities of the hyperelasticity-based damage theories for extreme stretch and failure in a natural rubbery material recently reported in Yu et al. (2020). They performed experiments on rubbery single-edge-notched specimens under mode-I tensile loading. The specimen width was 5 mm with a precrack length

of 1 mm. Moreover, the specimen height was 25 mm and the notch-root radius was 0.01 mm. The material parameters used in the numerical simulations with the three distinct driving forces for damage are listed in Table 7.

Fig. 10 shows the nominal stress-nominal strain curves of the natural rubbery specimen under large stretching in the experiments and numerical simulations. As shown in the experimental data (black solid line), final fracture occurs at a very large strain of ~ 7.3 ($\sim 730\%$ stretched). In the initial stage of tensile loading (up to a nominal strain of 2.0; ~ 200% stretched), the three simulation results with Gaussian entropy-driven, non-Gaussian entropy-driven and internal energydriven damage models are all in good agreement with the experimental stress-strain curve. Beyond an imposed tensile strain of 2.0, the dramatic hardening behavior observed in the experiment is captured by both of the non-Gaussian entropy-driven damage model (Arruda-Boyce) and internal energy-driven damage model (modified Arruda-Boyce with bond-stretching). The Gaussian entropy-driven damage model cannot describe the significant stress-upturn just before the specimen loses its load-bearing capacity. Additionally, the non-Gaussian entropy-driven damage model was unable to converge near total failure of the remaining ligament (see the red dashed stress-strain curve in Fig. 10). This may be attributed to all the free energy stored in the undamaged regions being released with no remaining contribution to constitutive behavior to receive. Furthermore, the extremely stiff, singular behavior near the limiting chain extensibility may lead to the additional convergence issue in the Arruda-Boyce model with no bond-stretching.

Notably, as demonstrated through the numerical simulations in the benchmark examples of the penny-shaped specimen and the double-edge-notched specimen in Section 4, as well as in the new example of the PMA elastomer in Fig. 9, both of the Gaussian entropy-driven and the non-Gaussian entropy-driven damage model with the very large locking stretch demonstrate an ability not only to capture the initial elastic response but also to predict the final fracture in elastomeric

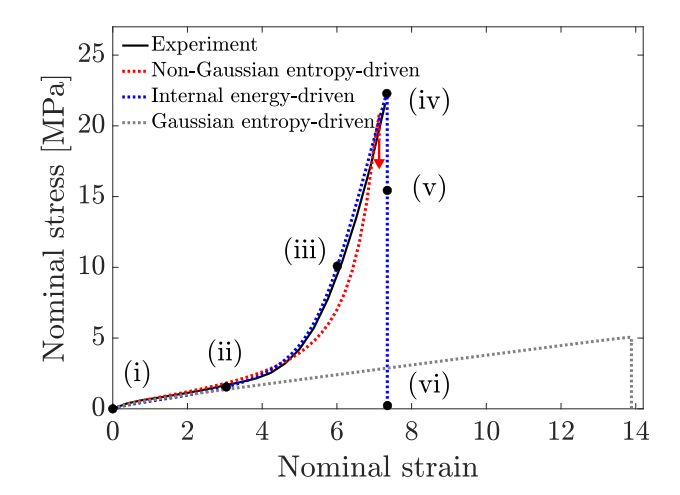


Fig. 10. Nominal stress vs. strain curves of a natural rubbery specimen in tension. Here, the solid line represents experimental data and the dashed lines represent simulation results with the Gaussian entropy-driven damage model (gray dashed line), non-Gaussian entropy-driven damage model (red dashed line) and internal energy-driven damage model (blue dashed line). (See Video S4 in the Supplemental Material).

 $^{^5}$ It should be noted that, in the microforce balance presented in Sections 2 and 3, the damage variable evolves when the entropic free energy is greater than $\epsilon_{\rm R}^f$ in the entropy-driven damage model while it evolves when the internal energy due to bond-stretching is greater than $\epsilon_{\rm R}^f$ in the internal energy-driven damage model.

 Table 7

 Material parameters used in simulations of a natural rubbery specimen in tension.

	μ [MPa]	K [MPa]	N	\bar{E}_b [MPa]	$\varepsilon_{\mathrm{R}}^{f}$ [MPa]	l [mm]	ζ [MPa s]
Non-Gaussian entropy-driven	0.38	350	22	N/A	70	0.5	50
Internal energy-driven	0.29	350	15	750	220	0.5	50
Gaussian entropy-driven	0.35	350	N/A	N/A	220	0.5	50

N/A: Not applicable.

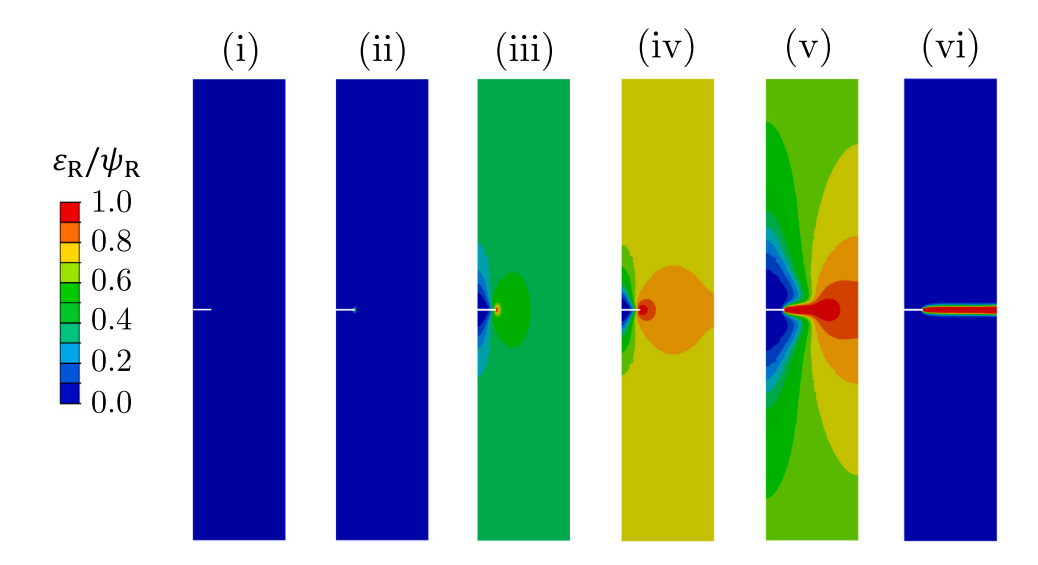


Fig. 11. Contours of the ratio of internal energy to the Helmholtz free energy in a natural rubbery specimen simulated with the internal energy-driven damage model. Contours are plotted on the reference configuration.

materials that fail at moderate stretch (e.g., ~ 130% in the double-edgenotched specimen example; ~ 200% in the PMA elastomer example). However, when the final rupture occurs at extreme stretch in the vicinity of the limiting chain extensibility in the materials (e.g., \sim 510% and $\sim 730\%$ in the single-notch specimen examples in Fig. 4 and Fig. 10, respectively), either internal energy-driven or non-Gaussian entropy-driven damage models should be employed to describe the remarkable hardening behavior due to the locking of chain networks. Further, note that the Gaussian or non-Gaussian entropy-driven damage models demonstrate the capabilities to model failure in elastomeric materials at moderate to large stretches with less computational efforts but neither of these models provide a physical picture during fracture processes. Rather, the internal energy-driven damage model presents more realistic descriptions of the failure that accompanies stretching and scission of molecular bonds throughout the chain networks at moderate (e.g., Fig. 9 on the PMA elastomer) to large stretches (e.g., Fig. 10 on the natural rubber), which is further illustrated in Fig. 11. It shows the contour plot of the ratio of the internal energy to the total Helmholtz free energy throughout the stretched natural rubbery specimen in the numerical simulation with the modified Arruda-Boyce with bondstretching examined in Fig. 10. Here, we plotted the contour with respect to the undeformed reference configuration in order to aid visualization. The internal energy-dominated region is limited in the vicinity of the notch tip at the early stage of tensile loading (ii); the majority of the specimen shows negligible internal energy. Then, as shown in stage (iii) in the contour plot, the majority of the specimen exhibits internal energy dominance (> 50% in the ratio) just before the crack propagates. The internal energy-dominated region increases as the crack propagates halfway through the specimen, as clearly shown in stages (iv) and (v). Finally, as the material loses its load-bearing capacity (vi), the ratio of the internal energy to the free energy recovers very rapidly throughout the entire specimen.

These two examples of synthetic and natural elastomers clearly demonstrated that the internal energy-driven model provides a more physical picture for failure in elastomers while both entropy- and

internal energy-driven damage models show excellent performance in predicting the failure at moderate to large stretches. Moreover, the entropy-driven damage models were found to be computationally more tractable when the failure occurs at a moderate stretch prior to locking. However, it should be noted that there are multiple layers of constitutive assumptions in these continuum damage models. Specifically, the elastomeric network was assumed to be ideal, by which the structural heterogeneity of non-uniform chain lengths and other topological features in realistic networks are not taken into account. Additionally, both entropy- and internal energy-driven damage models do not account for the statistical nature of damage criteria throughout the network. While these models demonstrated computational fidelity in predicting the failure in elastomers, there is much to further explore. More specifically, the statistical nature of damage throughout the realistic network topology should be incorporated for high-fidelity continuum-level constitutive models for damage and fracture.

6. Conclusion

In this work, we have presented a phase-field modeling framework based on the gradient-damage theory and associated computational procedures for extreme deformation events in elastomeric materials. The gradient-damage theories have been numerically implemented in a user-defined element (UEL) subroutine in Abaqus/Standard, for which we have discussed numerical solution procedures in significant detail. Furthermore, as found the online Supplemental materials of this paper, we have provided the source code and input files for all of the benchmark problems discussed in the paper. The details of numerical implementation and associated source codes will be useful in modeling of other diffusion-deformation types of multi-physics problems that accompany the extreme deformation and failure events in soft materials.

In addition to the computational details, we have discussed the gradient-damage theory with two distinct driving forces for damage:

(1) entropy-driven (the Gaussian entropy-based neo-Hookean and non-Gaussian entropy-based Arruda-Boyce) and (2) internal energy-driven (the modified Arruda-Boyce with bond-stretching) damage models. Notably, the purely Gaussian or non-Gaussian entropy-driven damage models demonstrated capabilities for fracture in elastomers at moderate to extreme stretch levels with much less computational efforts. However, the failure of elastomeric materials near the vicinity of the limiting chain extensibility was found to be better captured by the internal energy-driven damage model, which accounts for a more realistic physical picture of the stretching and scission of molecular bonds throughout the elastomeric network posited in the classical work by Lake and Thomas (1967).

As discussed in Section 5, we have employed the gradient-damage theories for idealized elastomeric networks in which all polymer chains are assumed to have the same length and deform homogeneously. However, the elastomer networks possess more complex topological features including poly-dispersion in the distribution of chain lengths and various molecular defects (Li and Bouklas, 2020; Vernerey, 2018; Vernerey et al., 2018; Zhong et al., 2016; Lin et al., 2019; Arora et al., 2020). Furthermore, the internal energy criterion is often insufficient, attributed to the probabilistic features of rupturing events in the elastomer networks. More recently, statistical mechanics frameworks have been employed to bring more realistic microscopic pictures in elastomer networks to the continuum-level constitutive model development (Buche and Silberstein, 2020, 2021; Buche et al., 2022; Mulderrig et al., 2023). In the future, the gradient-damage theory and its computational implementation can be further developed to better account for fracture processes in elastomeric materials with rigorous statistical mechanics considerations for more realistic elastomer networks with various topological features and molecular details. Furthermore, the nonlocal nature of fracture in elastomeric materials should be explored to extend the gradient-damage theory and its computational implementation to model elastomeric materials that exhibit size-dependent failure features across a wide range of length-scales. Inertial effects and dissipation mechanisms involving viscoelasticity and Mullins' effect in these materials can also be the focus of the next steps.

Declaration of competing interest

The authors declare the following financial interests/personal relationships which may be considered as potential competing interests: Hansohl Cho reports financial support was provided by National Research Foundation of Korea. Shawn A. Chester reports financial support was provided by National Science Foundation.

Data availability

Data will be made available on request.

Acknowledgments

We gratefully acknowledge valuable discussions with Yunwei Mao (Loopro Inc. and MIT). We are also grateful to Lallit Anand (MIT), who has read a preprint of this manuscript, for his helpful and constructive comments. A fruitful discussion with Jeongun Lee is also acknowledged. HC acknowledges financial support from the National Research Foundation of Korea under grant number (2020R1C1C101324813 and 2021R1A4A103278312). SAC acknowledges partial support from the National Science Foundation under grant numbers (CMMI-1463121 and CMMI-1751520).

Appendix A. Residuals and tangents in matrix form

We have developed four-noded isoparametric quadrilateral planestrain and plane-stress elements, and an eight-noded three-dimensional element. For each element type, we used specific matrix forms of the Piola stress, tangent modulus, and the gradient of the shape function. The displacement residuals and tangents are defined as shown below.

$$\begin{cases}
R_{\mathbf{u}} = -\int_{\mathcal{B}_{R}^{e}} G^{\mathsf{T}} S_{R} dv_{R} + \int_{S_{\mathbf{t}_{R}}^{e}} N^{\mathsf{T}} \check{\mathbf{t}}_{R} da_{R}, \\
K_{\mathbf{u}\mathbf{u}} = \int_{\mathcal{B}_{R}^{e}} G^{\mathsf{T}} A_{R} G dv_{R}
\end{cases}$$
(A.1)

with the matrix forms of the Piola stress S_R, tangent modulus A_R, and the standard gradient matrix of the shape function G.

A.1. Two-dimensional elements

For the plane-strain and plane-stress elements in two-dimensional analysis,

- The Piola stress vector $S_R = [T_{R,11} \ T_{R,21} \ T_{R,12} \ T_{R,22}]^{\top}$ The tangent modulus $(A_R)_{mn} = \left(\frac{\partial T_R}{\partial F}\right)_{ijkl}$ using the following transformation table

(i, j)	n	(k, l)
(1, 1)	1	(1, 1)
(2, 1)	2	(2, 1)
(1, 2)	3	(1, 2)
(2, 2)	4	(2, 2)
	(1, 1) (2, 1) (1, 2)	(1, 1) 1 (2, 1) 2 (1, 2) 3

For the plane-stress element, the tangent modulus is statically condensed

$$A_{ps} = A_{R} - A_{R12}^{\mathsf{T}} A_{R22}^{-1} A_{R,21}$$
 (A.2)

$$\begin{split} &\mathsf{A}_{ps} = \mathsf{A}_{R} - \mathsf{A}_{R,12} \, \mathsf{A}_{R,22} \, \mathsf{A}_{R,21} \\ &\mathsf{where} \ \ \mathsf{A}_{R,12} \! = \! \left[\frac{\partial \mathsf{T}_{R,11}}{\partial \mathsf{F}_{33}} \, \frac{\partial \mathsf{T}_{R,21}}{\partial \mathsf{F}_{33}} \, \frac{\partial \mathsf{T}_{R,12}}{\partial \mathsf{F}_{33}} \, \frac{\partial \mathsf{T}_{R,22}}{\partial \mathsf{F}_{33}} \, \right] , \ \ \mathsf{A}_{R,21} \! = \! \left[\frac{\partial \mathsf{T}_{R,33}}{\partial \mathsf{F}_{11}} \, \frac{\partial \mathsf{T}_{R,33}}{\partial \mathsf{F}_{21}} \, \frac{\partial \mathsf{T}_{R,33}}{\partial \mathsf{F}_{22}} \, \frac{\partial \mathsf{T}_{R,33}}{\partial \mathsf{F}_{22}} \right] , \\ &\mathsf{and} \ \ \mathsf{A}_{R,22} = \left[\frac{\partial \mathsf{T}_{R,33}}{\partial \mathsf{F}_{33}} \right] . \end{split}$$

• G-matrix where M is the total number of nodes per element

$$G = \begin{bmatrix} \frac{\partial N^{1}}{\partial X_{1}} & 0 & \frac{\partial N^{2}}{\partial X_{1}} & 0 & \cdots & \frac{\partial N^{M}}{\partial X_{1}} & 0\\ 0 & \frac{\partial N^{1}}{\partial X_{1}} & 0 & \frac{\partial N^{2}}{\partial X_{1}} & \cdots & 0 & \frac{\partial N^{M}}{\partial X_{1}} \\ \frac{\partial N^{1}}{\partial X_{2}} & 0 & \frac{\partial N^{2}}{\partial X_{2}} & 0 & \cdots & \frac{\partial N^{M}}{\partial X_{2}} & 0\\ 0 & \frac{\partial N^{1}}{\partial X_{2}} & 0 & \frac{\partial N^{2}}{\partial X_{2}} & \cdots & 0 & \frac{\partial N^{M}}{\partial X_{2}} \end{bmatrix}$$

$$(A.3)$$

Element-level residuals and tangents in matrix forms, denoted as RHS and AMATRX, in Abaqus/ Standard for each iteration are defined as follows:

• Residuals (dimension of $1 \times 3M$) $RHS = \begin{bmatrix} R_{u_1}^1 R_{u_2}^1 R_d^1 \cdots R_{u_1}^M R_{u_2}^M R_d^M \end{bmatrix}$ (A.4)

• Tangents (dimension of $3M \times 3M$)

$$\text{AMATRX} = \begin{bmatrix} K_{u_1u_1}^{11} & K_{u_1u_2}^{11} & K_{u_1d}^{11} & \cdots & K_{u_1u_1}^{1M} & K_{u_1u_2}^{1M} & K_{u_1d}^{1M} \\ K_{u_2u_1}^{11} & K_{u_2u_2}^{11} & K_{u_2d}^{11} & \cdots & K_{u_2u_1}^{1M} & K_{u_2u_2}^{1M} & K_{u_2d}^{1M} \\ K_{du_1}^{11} & K_{du_2}^{11} & K_{dd}^{11} & \cdots & K_{du_1}^{1M} & K_{du_2}^{1M} & K_{dd}^{1M} \\ \vdots & \vdots & & \vdots & & \vdots & \vdots \\ K_{u_1u_1}^{M1} & K_{u_1u_2}^{M1} & K_{u_1d}^{M1} & \cdots & K_{u_1u_1}^{MM} & K_{u_1u_2}^{MM} & K_{u_1d}^{MM} \\ K_{u_2u_1}^{M1} & K_{u_2u_2}^{M1} & K_{u_2d}^{M1} & \cdots & K_{u_2u_1}^{MM} & K_{u_2u_2}^{MM} & K_{u_2d}^{MM} \\ K_{du_1}^{M1} & K_{du_2}^{M1} & K_{dd}^{M1} & \cdots & K_{du_1}^{MM} & K_{du_2}^{MM} & K_{dd}^{MM} \end{bmatrix}$$

$$(A.5)$$

A.2. Three-dimensional elements

For the eight-noded three-dimensional element,

- The Piola stress vector $S_R = [T_{R,11} \ T_{R,21} \ T_{R,31} \ T_{R,12} \ T_{R,22} \ T_{R,32} \ T_{R,31}]^\top$
- The tangent modulus $(A_R)_{mn} = \left(\frac{\partial T_R}{\partial F}\right)_{ijkl}$ using the following transformation table

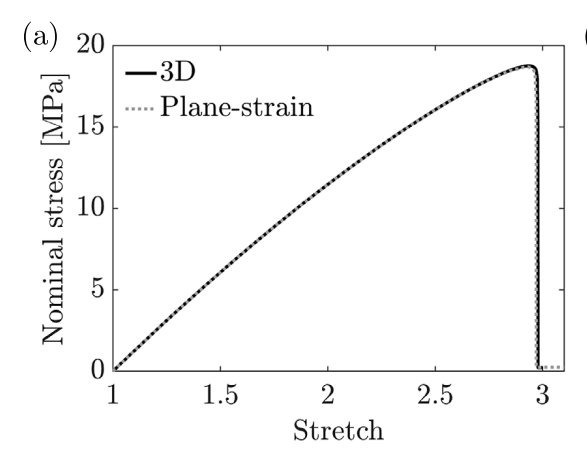
m	(i, j)	n	(k, l)
1	(1, 1)	1	(1, 1)
2	(2, 1)	2	(2, 1)
3	(3, 1)	3	(3, 1)
4	(1, 2)	4	(1, 2)
5	(2, 2)	5	(2, 2)
6	(3, 2)	6	(3, 2)
7	(1, 3)	7	(1, 3)
8	(2, 3)	8	(2, 3)
9	(3, 3)	9	(3, 3)

· G-matrix

Then, the element-level residuals and tangents in matrix forms, RHS and AMATRX are given,

• Residuals (dimension of $1 \times 4M$)

$$RHS = \left[R_{u_1}^1 R_{u_2}^1 R_{u_3}^1 R_d^1 \cdots R_{u_1}^M R_{u_2}^M R_{u_3}^M R_d^M \right]$$
(A.7)



• Tangents (dimension of $4M \times 4M$)

A.3. Verification of 2D and 3D elements

For verification of the two- and three-dimensional elements, we compare the numerical simulation results of single-edge-notched specimens using the plane-strain and the plane-stress elements against those with the three-dimensional elements. As shown in Fig. A.1, the nominal stress-stretch curves using the three-dimensional elements nicely matched those with (a) the plane-strain elements and (b) the plane-stress elements. For the plane-strain case with the three-dimensional elements, the dimension in thickness direction has been constrained to be constant. Furthermore, for the plane-stress case with the three-dimensional elements, the thickness has been taken to be much smaller than in-plane dimensions with only a few elements.

Appendix B. F-bar method

Here, we provide details of the residuals and tangents for *F-bar* elements in the reference formulation in de Souza Neto et al. (1996).⁶ We define the *F-bar* deformation gradient as

$$\bar{\mathbf{F}} = \left(\frac{\det \mathbf{F}_0}{\det \mathbf{F}}\right)^{1/3} \mathbf{F} \tag{B.1}$$

 $^{^{6}}$ In their paper, a general procedure for the formulation of F-bar elements in a spatial configuration is provided.

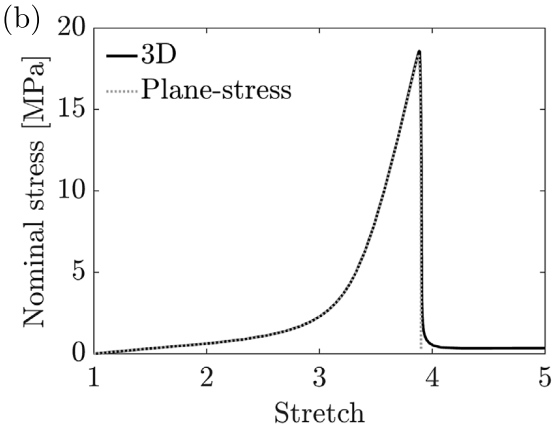


Fig. A.1. Nominal stress vs. stretch curves for (a) double-edge-notched specimen: 3D vs. plane-strain elements (see Fig. 5) and (b) single-edge-notched specimen: 3D vs. plane-strain elements (see Fig. 3).

where \mathbf{F}_0 is the deformation gradient at the centroid of the element. Then, the first Piola stress is

$$\begin{split} \mathbf{T}_{\mathbf{R}} &= J\mathbf{T}\mathbf{F}^{-\top} = J\hat{\mathbf{T}}(\bar{\mathbf{F}})\mathbf{F}^{-\top} \\ &= \left(\frac{\det \mathbf{F}_{0}}{\det \mathbf{F}}\right)^{-2/3}\hat{\mathbf{T}}_{\mathbf{R}}(\bar{\mathbf{F}}). \end{split} \tag{B.2}$$

Then, we obtain the residual in terms of $\bar{\mathbf{F}}$,

$$\mathbf{R_{u}} = -\int_{B_{p}^{e}} \left(\frac{\det \mathbf{F}_{0}}{\det \mathbf{F}}\right)^{-2/3} \hat{\mathbf{T}}_{R}(\bar{\mathbf{F}}) \frac{\partial N^{A}}{\partial \mathbf{X}} dv_{R}. \tag{B.3}$$

The tangent in terms of $\bar{\mathbf{F}}$ is given by

$$\begin{split} K_{u_{i}u_{k}}^{AB} &= \int_{B_{R}^{e}} \frac{\partial N^{A}}{\partial X_{j}} \, \frac{\partial}{\partial F_{kl}} \left[\left(\frac{\det \mathbf{F}_{0}}{\det \mathbf{F}} \right)^{-2/3} \hat{T}_{R}(\bar{\mathbf{F}})_{ij} \right] \frac{\partial N^{B}}{\partial X_{l}} \, dv_{R} \\ &= \int_{B_{R}^{e}} \frac{\partial N^{A}}{\partial X_{j}} \, \left[\left(\frac{\det \mathbf{F}_{0}}{\det \mathbf{F}} \right)^{-1/3} \, \frac{\partial \hat{T}_{R}(\bar{\mathbf{F}})_{ij}}{\partial \bar{F}_{kl}} \right] \frac{\partial N^{B}}{\partial X_{l}} \, + \, \frac{\partial N^{A}}{\partial X_{j}} \left(\frac{\det \mathbf{F}_{0}}{\det \mathbf{F}} \right)^{-2/3} \times \\ &\left[\frac{1}{3} \, \frac{\partial \hat{T}_{R}(\bar{\mathbf{F}})_{ij}}{\partial \bar{F}_{mn}} \, \bar{F}_{mn} \left(F_{0,kl}^{-\intercal} \, \frac{\partial N_{0}^{B}}{\partial X_{l}} - F_{kl}^{-\intercal} \, \frac{\partial N^{B}}{\partial X_{l}} \right) \right. \\ &\left. - \frac{2}{3} \, \hat{T}_{R}(\bar{\mathbf{F}})_{ij} \left(F_{0,kl}^{-\intercal} \, \frac{\partial N_{0}^{B}}{\partial X_{l}} - F_{kl}^{-\intercal} \, \frac{\partial N^{B}}{\partial X_{l}} \right) \right] dv_{R}. \end{split} \tag{B.4}$$

It can be expressed in a matrix form as

$$\mathsf{K}_{\mathbf{u}\mathbf{u}} = \int_{\mathcal{B}_{\mathsf{R}}^{\mathsf{F}}} \left[\left(\frac{\det \mathbf{F}_0}{\det \mathbf{F}} \right)^{-1/3} \mathsf{G}^{\mathsf{T}} \mathsf{A}_{\mathsf{R}} \mathsf{G} \right. \\ \left. + \left(\frac{\det \mathbf{F}_0}{\det \mathbf{F}} \right)^{-2/3} \mathsf{G}^{\mathsf{T}} (\mathsf{Q}_{\mathsf{R}0} \mathsf{G}_0 - \mathsf{Q}_{\mathsf{R}} \mathsf{G}) \right] \, dv_{\mathsf{R}}$$
 (B.5)

where $\mathsf{A}_R,\,\mathsf{Q}_R$ and Q_{R0} are the matrix forms of the fourth-order tensors $\mathbb{A}_R=\frac{\partial \hat{T}_R(\bar{F})}{\partial \bar{F}},$

$$\mathbb{Q}_{R} = \frac{1}{3} \mathbb{A}_{R} : (\bar{\mathbf{F}} \otimes \mathbf{F}^{-\mathsf{T}}) - \frac{2}{3} \mathbf{T}_{R} (\bar{\mathbf{F}}) \otimes \mathbf{F}^{-\mathsf{T}} \quad \text{and}
\mathbb{Q}_{R0} = \frac{1}{3} \mathbb{A}_{R} : (\bar{\mathbf{F}} \otimes \mathbf{F}_{0}^{-\mathsf{T}}) - \frac{2}{3} \mathbf{T}_{R} (\bar{\mathbf{F}}) \otimes \mathbf{F}_{0}^{-\mathsf{T}}. \tag{B.6}$$

Similarly, we define the F-bar deformation gradient in a 2D planestrain situation as

$$\bar{\mathbf{F}} = \begin{bmatrix} & & & 0 \\ & \bar{\mathbf{F}}_{pe} & & 0 \\ & & 0 & 1 \end{bmatrix} \quad \text{where} \quad \bar{\mathbf{F}}_{pe} = \left(\frac{\det \mathbf{F}_0}{\det \mathbf{F}}\right)^{1/2} \mathbf{F}$$
 (B.7)

Hence, the residual is expressed as

$$\mathbf{R}_{\mathbf{u}} = -\int_{\mathcal{B}_{\mathbf{c}}^{c}} \left(\frac{\det \mathbf{F}_{0}}{\det \mathbf{F}}\right)^{-1/2} \hat{\mathbf{T}}_{\mathbf{R}}(\bar{\mathbf{F}}) \frac{\partial N^{A}}{\partial \mathbf{X}} dv_{\mathbf{R}}.$$
 (B.8)

Then, the tangent is given by

$$\begin{split} K_{u_{i}u_{k}}^{AB} &= \int_{B_{\mathbf{r}}^{e}} \frac{\partial N^{A}}{\partial X_{j}} \, \frac{\partial}{\partial F_{kl}} \left[\left(\frac{\det \mathbf{F}_{0}}{\det \mathbf{F}} \right)^{-1/2} \hat{T}_{\mathbf{R}}(\bar{\mathbf{F}})_{ij} \right] \frac{\partial N^{B}}{\partial X_{l}} \, dv_{\mathbf{R}} \\ &= \int_{B_{\mathbf{r}}^{e}} \frac{\partial N^{A}}{\partial X_{j}} \, \frac{\partial \hat{T}_{\mathbf{R}}(\bar{\mathbf{F}})_{ij}}{\partial \bar{F}_{kl}} \, \frac{\partial N^{B}}{\partial X_{l}} + \frac{\partial N^{A}}{\partial X_{j}} \left(\frac{\det \mathbf{F}_{0}}{\det \mathbf{F}} \right)^{-1/2} \times \\ &\left[\frac{1}{2} \, \frac{\partial \hat{T}_{\mathbf{R}}(\bar{\mathbf{F}})_{ij}}{\partial \bar{F}_{mn}} \, \bar{F}_{mn} \left(F_{0,kl}^{-\mathsf{T}} \, \frac{\partial N^{B}}{\partial X_{l}} - F_{kl}^{-\mathsf{T}} \, \frac{\partial N^{B}}{\partial X_{l}} \right) \right. \\ &\left. - \frac{1}{2} \hat{T}_{\mathbf{R}}(\bar{\mathbf{F}})_{ij} \left(F_{0,kl}^{-\mathsf{T}} \, \frac{\partial N^{B}}{\partial X_{l}} - F_{kl}^{-\mathsf{T}} \, \frac{\partial N^{B}}{\partial X_{l}} \right) \right] \, dv_{\mathbf{R}}. \end{split} \tag{B.9}$$

The matrix form for the tangent is given by

$$\mathsf{K}_{\mathbf{u}\mathbf{u}} = \int_{B_{\mathsf{R}}^e} \left[\mathsf{G}^\mathsf{T} \mathsf{A}_\mathsf{R} \mathsf{G} + \left(\frac{\det \mathbf{F}_0}{\det \mathbf{F}} \right)^{-1/2} \mathsf{G}^\mathsf{T} (\mathsf{Q}_{\mathsf{R}0} \mathsf{G}_0 - \mathsf{Q}_\mathsf{R} \mathsf{G}) \right] dv_\mathsf{R} \qquad (B.10)$$

where

$$\begin{split} \mathbb{Q}_R &= \frac{1}{2} \mathbb{A}_R \, : \, (\bar{\mathbf{F}} \otimes \mathbf{F}^{-\top}) - \frac{1}{2} \mathbf{T}_R (\bar{\mathbf{F}}) \otimes \mathbf{F}^{-\top} \quad \text{and} \\ \mathbb{Q}_{R0} &= \frac{1}{2} \mathbb{A}_R \, : \, (\bar{\mathbf{F}} \otimes \mathbf{F}_0^{-\top}) - \frac{1}{2} \mathbf{T}_R (\bar{\mathbf{F}}) \otimes \mathbf{F}_0^{-\top}. \end{split} \tag{B.11}$$

The spatial F-bar formulation in detail can also be found in Chester et al. (2015).

Appendix C. Analytical vs. numerical tangent

Here, we verify the analytical tangent modulus presented in Section 3.3 by comparing the simulation results against those with the

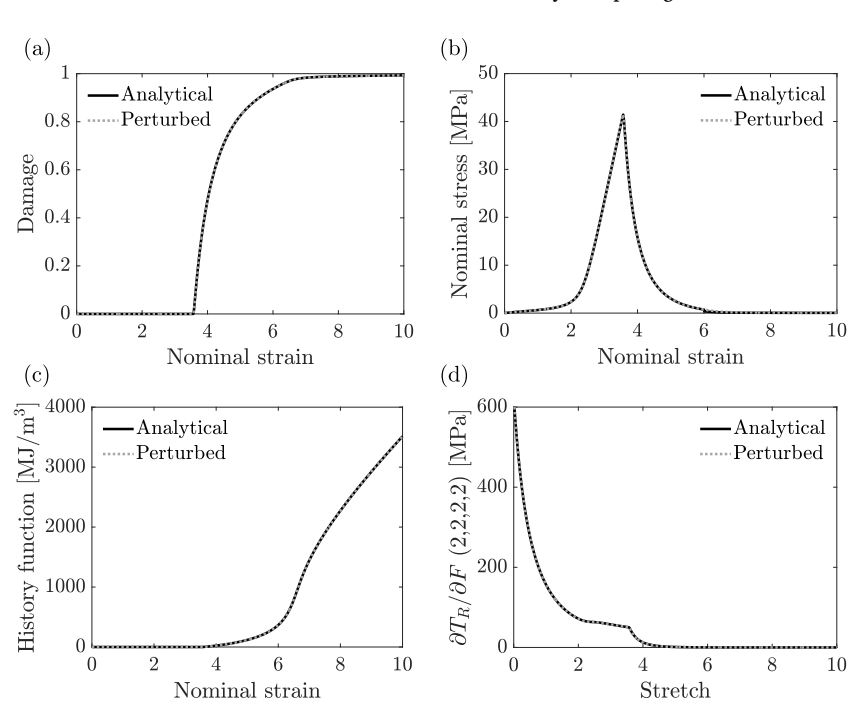


Fig. C.1. Comparisons of simulation results on one element in tension using analytical and perturbed tangent moduli: (a) damage variable, (b) nominal stress, (c) history function, and (d) (2,2,2,2) component of the tangent moduli.

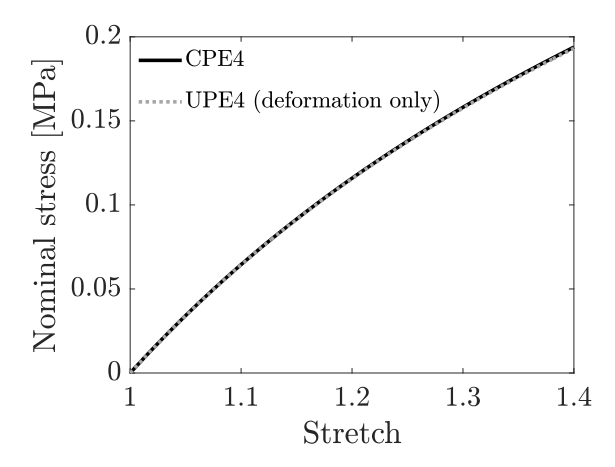


Fig. D.1. Nominal stress vs. stretch curves in double-edge-notched specimens in tension using the Abaqus built-in element (CPE4) and UEL (UPE4) using the nearly incompressible neo-Hookean model.

numerical tangent modulus obtained by perturbing the deformation gradient. A perturbed deformation gradient is given by

$$\mathbf{F}_{n+1}^{\text{per},kl} = \mathbf{F}_{n+1} + \Delta \mathbf{F}^{kl} \tag{C.1}$$

where the perturbation is defined as

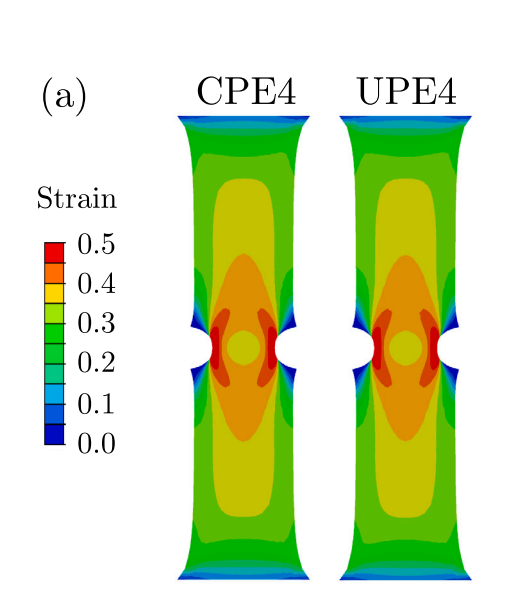
$$\Delta \mathbf{F}^{kl} = \Delta \epsilon \, \mathbf{e}_k \otimes \mathbf{e}_l \tag{C.2}$$

with the Cartesian basis, $\mathbf{e}_{i=1,2,3}$. Then, the numerical tangent modulus is calculated by

$$\left(\frac{\partial \mathbf{T}_{R}}{\partial \mathbf{F}}\right)_{ijkl} = \frac{T_{R,ij}(\mathbf{F}_{n+1}^{\text{per},kl}) - T_{R,ij}(\mathbf{F}_{n+1}^{kl})}{\Delta\epsilon}.$$
(C.3)

In Fig. C.1, one-element simulation results with the analytical tangent modulus (solid lines) are compared against those with the numerical tangent modulus (dashed lines). We showed that (a) the damage variable, (b) the nominal stress, (c) the history function, and (d) the (2,2,2,2) component of the tangent modulus nicely matched those in numerical simulations with a perturbed, numerical tangent modulus.

Appendix D. Verification of plane-strain and plane-stress elements: Deformation-only problems



We briefly compare the simulation results of the "deformation only" problems using UEL subroutines against those simulated with the built-in elements in Abaqus/Standard. First, we consider a two-dimensional plane-strain element, referred to as UPE4, in our UEL implementation and an Abaqus/Standard plane-strain element, referred to as CPE4. In Fig. D.1, the nominal stress–stretch curves of double-edge-notched specimens using UPE4 and CPE4 are shown; furthermore, the contours of axial strain and stress fields are displayed in Fig. D.2. Here, we used the nearly incompressible neo-Hookean model. As shown, the simulation results with UPE4 elements match nicely those with the CPE4 elements.

We then verify the two-dimensional plane-stress element in our UEL subroutines (UPS4) by comparing the simulation results of single-edge-notched specimens with UPS4 elements against those with an Abaqus/Standard plane-strain element, CPS4. Here, we used the nearly incompressible Arruda-Boyce model with no bond-stretching for brevity. In Fig. D.3, the nominal stress–stretch curves of single-edge-notched specimens using UPS4 and CPS4 are shown; furthermore, the contours of axial strain and stress fields are displayed in Fig. D.4. As shown, the simulation results with UPS4 elements match nicely those with the CPS4 elements.

Appendix E. Updating stress and tangent in compressible hyperelastic materials

In this section, we provide the stresses and tangents for the compressible versions of a neo-Hookean model with no bond-stretching and a modified Arruda-Boyce model with bond-stretching for completeness.

1. Compressible neo-Hookean: Purely (Gaussian) entropy-driven damage model

The first Piola stress is

$$\mathbf{T}_{\mathbf{R}} = \left[(1 - d)^2 + k \right] \left[\mu \left(\mathbf{F} - \mathbf{F}^{-\top} \right) + K(J - 1)J\mathbf{F}^{-\top} \right]. \tag{E.1}$$

The referential tangent modulus, $\frac{\partial \mathbf{T}_{R}}{\partial \mathbf{F}}$ is then given by,

$$\begin{split} &\frac{\partial \left(T_{\rm R}\right)_{ij}}{\partial F_{kl}} = \left[(1-d)^2 + k \right] \left[\mu \left(\delta_{ik} \delta_{jl} + F_{li}^{-1} F_{jk}^{-1} \right) \right. \\ &\left. + K \left\{ (2J-1)J F_{kl}^{-\top} F_{ij}^{-\top} - (J-1)J F_{li}^{-1} F_{jk}^{-1} \right\} \right]. \end{split} \tag{E.2}$$

2. Compressible, modified Arruda-Boyce: Internal energy-driven damage model

The first Piola stress is

$$\mathbf{T}_{R} = \bar{\mu} \left(\mathbf{F} - \mathbf{F}^{-\top} \right) + \left[(1 - d)^{2} + k \right] K(J - 1) J \mathbf{F}^{-\top}$$
 (E.3)

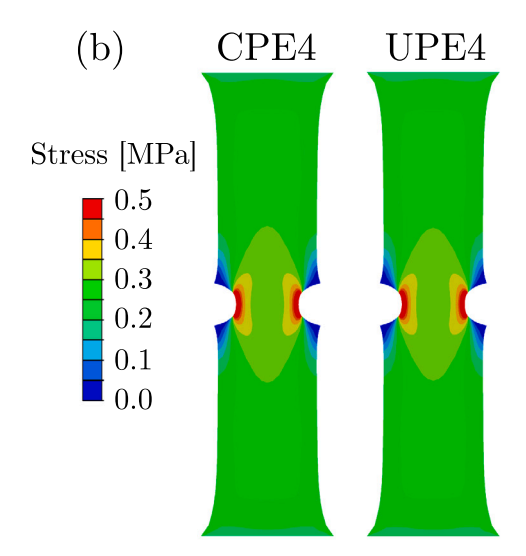


Fig. D.2. Contours of (a) axial strain and (b) axial stress using CPE4 and UPE4 elements. Contours are plotted on deformed configurations at a stretch of 1.4.

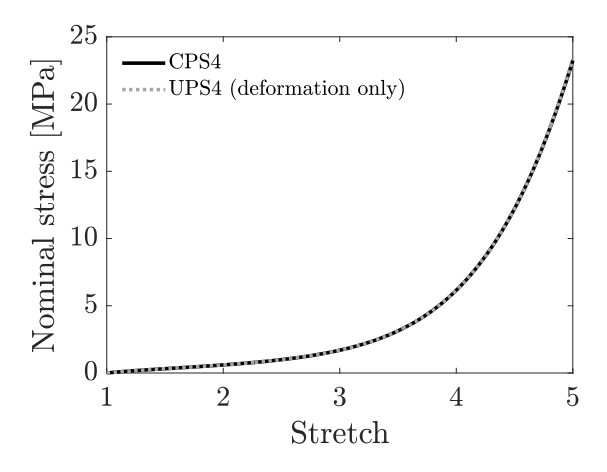


Fig. D.3. Nominal stress vs. stretch curves in single-edge-notched specimens in tension using the Abaqus built-in element (CPS4) and UEL subroutine (UPS4) using the nearly incompressible Arruda-Boyce model with no bond-stretching.

where $\bar{\mu}=\frac{\mu}{3}\frac{\sqrt{n}}{\bar{\lambda}\lambda_b}\mathcal{L}^{-1}\left(\frac{\bar{\lambda}}{\lambda_b\sqrt{n}}\right)$ and $\bar{\lambda}=\sqrt{\frac{1}{3}}\text{tr}\mathbf{C}$. Then, the referential tangent modulus, $\frac{\partial \mathbf{T}_{\mathbf{R}}}{\partial \mathbf{F}}$ is given by

$$\frac{\partial \left(T_{R}\right)_{ij}}{\partial F_{kl}}\bigg|_{d} = \frac{\partial \left(T_{R}\right)_{ij}}{\partial F_{kl}}\bigg|_{\lambda_{k},d} + \frac{\partial \left(T_{R}\right)_{ij}}{\partial \lambda_{b}}\bigg|_{E,d} \frac{\partial \lambda_{b}}{\partial F_{kl}}\bigg|_{d}. \tag{E.4}$$

Then, we have

$$\begin{split} \frac{\partial \left(T_{\mathrm{R}}\right)_{ij}}{\partial F_{kl}} \bigg|_{\lambda_{b},d} &= \quad \bar{\mu} \left(\delta_{ik} \delta_{jl} + F_{ll}^{-1} F_{jk}^{-1} \right) + \frac{\partial \bar{\mu}}{\partial F_{kl}} \left(F_{ij} - F_{ij}^{-\top} \right) \\ &+ \quad \left[(1-d)^{2} + k \right] K \left[(2J-1)J F_{kl}^{-\top} F_{ij}^{-\top} - (J-1)J F_{ll}^{-1} F_{jk}^{-1} \right], \\ \frac{\partial \left(T_{\mathrm{R}}\right)_{ij}}{\partial \lambda_{b}} \bigg|_{\mathrm{F},d} &= \quad \frac{\partial \bar{\mu}}{\partial \lambda_{b}} \left(F_{ij} - F_{ij}^{-\top} \right), \end{split}$$

where the three terms $\frac{\partial \bar{\mu}}{\partial E_{t,t}}$, $\frac{\partial \bar{\mu}}{\partial \lambda_{b,t}}$, $\frac{\partial \lambda_{b,t}}{\partial E_{t,t}}$ are given in Section 3.3.

Strain

1.0
0.8
0.6
0.4
0.2
0.0

Appendix F. An example of a mesh in deformed configuration

Here, we provide sequential images of the damaged elements in the double-edge notched specimen in deformed configuration presented in Section 4.3 (see Fig. F.1). It should be noted that the gradient-damage model nicely captures the crack initiation, propagation, and full rupture processes throughout the specimen without any mesh refinement.

Appendix G. Supplementary data

Supplementary material related to this article can be found online at https://doi.org/10.1016/j.ijsolstr.2023.112309.

References

Alnæs, M., Blechta, J., Hake, J., Johansson, A., Kehlet, B., Logg, A., Richardson, C., Ring, J., Rognes, M.E., Wells, G.N., 2015. The FEniCS project version 1.5. Arch. Numer. Softw. 3 (100).

Alnæs, M.S., Logg, A., Ølgaard, K.B., Rognes, M.E., Wells, G.N., 2014. Unified form language: A domain-specific language for weak formulations of partial differential equations. ACM Trans. Math. Softw. 40 (2), 1–37.

Arora, A., Lin, T.-S., Beech, H.K., Mochigase, H., Wang, R., Olsen, B.D., 2020. Fracture of polymer networks containing topological defects. Macromolecules 53 (17), 7346–7355.

Arruda, E.M., Boyce, M.C., 1993. A three-dimensional constitutive model for the large stretch behavior of rubber elastic materials. J. Mech. Phys. Solids 41 (2), 389–412.
 Bourdin, B., Francfort, G.A., Marigo, J.J., 2000. Numerical experiments in revisited brittle fracture. J. Mech. Phys. Solids 48 (4), 797–826.

Buche, M.R., Silberstein, M.N., 2020. Statistical mechanical constitutive theory of polymer networks: The inextricable links between distribution, behavior, and ensemble. Phys. Rev. E 102 (1), 012501.

Buche, M.R., Silberstein, M.N., 2021. Chain breaking in the statistical mechanical constitutive theory of polymer networks. J. Mech. Phys. Solids 156, 104593.

Buche, M.R., Silberstein, M.N., Grutzik, S.J., 2022. Freely jointed chain models with extensible links. Phys. Rev. E 106 (2), 024502.

Chen, C., Wang, Z., Suo, Z., 2017. Flaw sensitivity of highly stretchable materials. Extreme Mech. Lett. 10, 50–57.

Chester, S.A., Anand, L., 2010. A coupled theory of fluid permeation and large deformations for elastomeric materials. J. Mech. Phys. Solids 58 (11), 1879–1906.

Chester, S.A., Di Leo, C.V., Anand, L., 2015. A finite element implementation of a coupled diffusion-deformation theory for elastomeric gels. Int. J. Solids Struct. 52, 1–18

Creton, C., 2017. 50th anniversary perspective: Networks and gels: Soft but dynamic and tough. Macromolecules 50 (21), 8297–8316.

de Borst, R., 2002. Fracture in quasi-brittle materials: a review of continuum damage-based approaches. Eng. Fract. Mech. 69 (2), 95–112.

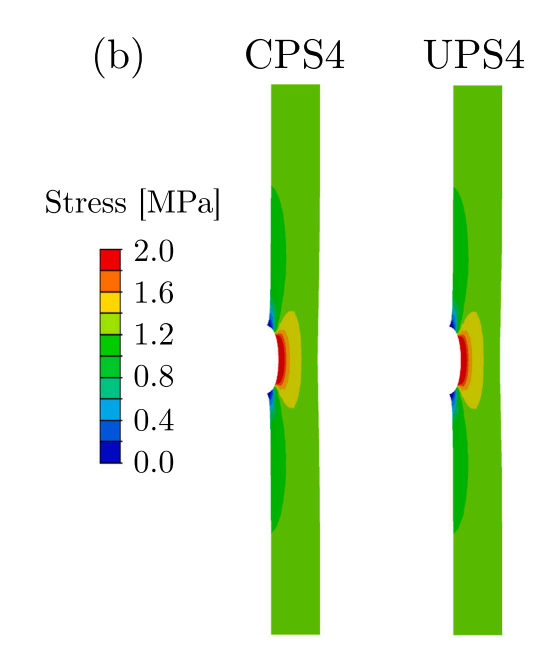


Fig. D.4. Contours of (a) axial strain and (b) axial stress using CPS4 and UPS4 elements. Contours are plotted on deformed configurations at a stretch of 3.

(E.5)

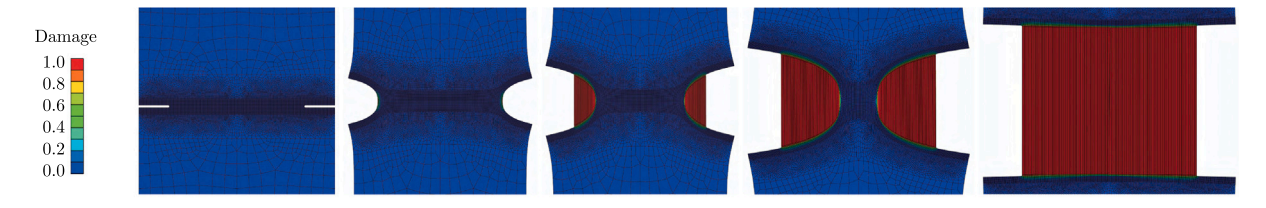


Fig. F.1. Contour plot on a damage field in severely damaged elements in the deformed mesh of the double-edge notched specimen presented in Section 4.3.

- de Borst, R., Pamin, J., Geers, M.G.D., 1999. On coupled gradient-dependent plasticity and damage theories with a view to localization analysis. Eur. J. Mech. A Solids 18 (6) 939-962
- de Borst, R., Verhoosel, C.V., 2016. Gradient damage vs phase-field approaches for fracture: Similarities and differences. Comput. Methods Appl. Mech. Engrg. 312, 78, 04
- de Souza Neto, E.A., Perić, D., Dutko, M., Owen, D.R.J., 1996. Design of simple low order finite elements for large strain analysis of nearly incompressible solids. Int. J. Solids Struct. 33 (20–22), 3277–3296.
- Di Leo, C.V., Rejovitzky, E., Anand, L., 2014. A Cahn-Hilliard-type phase-field theory for species diffusion coupled with large elastic deformations: application to phase-separating Li-ion electrode materials. J. Mech. Phys. Solids 70, 1–29.
- Francfort, G.A., Marigo, J.J., 1998. Revisiting brittle fracture as an energy minimization problem. J. Mech. Phys. Solids 46 (8), 1319–1342.
- Frémond, M., Nedjar, B., 1996. Damage, gradient of damage and principle of virtual power. Int. J. Solids Struct. 33 (8), 1083–1103.
- Gültekin, O., Dal, H., Holzapfel, G.A., 2016. A phase-field approach to model fracture of arterial walls: theory and finite element analysis. Comput. Methods Appl. Mech. Engrg. 312. 542–566.
- Gurtin, M.E., 1996. Generalized Ginzburg-Landau and Cahn–Hilliard equations based on a microforce balance. Physica D 92 (3–4), 178–192.
- Henann, D.L., Chester, S.A., Bertoldi, K., 2013. Modeling of dielectric elastomers: Design of actuators and energy harvesting devices. J. Mech. Phys. Solids 61 (10), 2047–2066.
- Henann, D.L., Kamrin, K., 2016. A finite element implementation of the nonlocal granular rheology. Internat. J. Numer. Methods Engrg. 108 (4), 273–302.
- Hocine, N.A., Abdelaziz, M.N., Imad, A., 2002. Fracture problems of rubbers: J-integral estimation based upon η factors and an investigation on the strain energy density distribution as a local criterion. Int. J. Fract. 117 (1), 1–23.
- Hofacker, M., Miehe, C., 2012. Continuum phase field modeling of dynamic fracture: variational principles and staggered FE implementation. Int. J. Fract. 178 (1), 113–129.
- Klinkel, S., Govindjee, S., 2002. Using finite strain 3D-material models in beam and shell elements. Eng. Comput. 19 (3), 254–271.
- Konica, S., Sain, T., 2021. A homogenized large deformation constitutive model for high temperature oxidation in fiber-reinforced polymer composites. Mech. Mater. 160, 103994.
- Kristensen, P.K., Martínez-Pañeda, E., 2020. Phase field fracture modelling using quasi-Newton methods and a new adaptive step scheme. Theor. Appl. Fract. Mech. 107, 102446
- Kumar, A., Bourdin, B., Francfort, G.A., Lopez-Pamies, O., 2020. Revisiting nucleation in the phase-field approach to brittle fracture. J. Mech. Phys. Solids 142, 104027.
- Kumar, A., Francfort, G.A., Lopez-Pamies, O., 2018. Fracture and healing of elastomers: A phase-transition theory and numerical implementation. J. Mech. Phys. Solids 112, 523–551.
- Lake, G.J., Thomas, A.G., 1967. The strength of highly elastic materials. Proc. R. Soc. Lond. Ser. A Math. Phys. Eng. Sci. 300 (1460), 108–119.
- Li, B., Bouklas, N., 2020. A variational phase-field model for brittle fracture in polydisperse elastomer networks. Int. J. Solids Struct. 182, 193–204.
- Lin, T.-S., Wang, R., Johnson, J.A., Olsen, B.D., 2019. Revisiting the elasticity theory for real Gaussian phantom networks. Macromolecules 52 (4), 1685–1694.
- Long, R., Hui, C.-Y., Gong, J.P., Bouchbinder, E., 2021. The fracture of highly deformable soft materials: A tale of two length scales. Annu. Rev. Condens. Matter Phys. 12, 71–94.
- Lorentz, E., Andrieux, S., 1999. A variational formulation for nonlocal damage models. Int. J. Plast. 15 (2), 119–138.
- Lorentz, E., Godard, V., 2011. Gradient damage models: Toward full-scale computations. Comput. Methods Appl. Mech. Engrg. 200 (21–22), 1927–1944.
- Mandal, T.K., Gupta, A., Nguyen, V.P., Chowdhury, R., de Vaucorbeil, A., 2020. A length scale insensitive phase field model for brittle fracture of hyperelastic solids. Eng. Fract. Mech. 236, 107196.

- Mao, Y., Anand, L., 2018a. Fracture of elastomeric materials by crosslink failure. J. Appl. Mech. 85 (8).
- Mao, Y., Anand, L., 2018b. A theory for fracture of polymeric gels. J. Mech. Phys. Solids 115, 30–53.
- Mao, Y., Talamini, B., Anand, L., 2017. Rupture of polymers by chain scission. Extreme Mech. Lett. 13, 17–24.
- Miehe, C., Hofacker, M., Welschinger, F., 2010a. A phase field model for rate-independent crack propagation: Robust algorithmic implementation based on operator splits. Comput. Methods Appl. Mech. Engrg. 199 (45–48), 2765–2778.
- Miehe, C., Schaenzel, L.-M., Ulmer, H., 2015. Phase field modeling of fracture in multiphysics problems. Part I. Balance of crack surface and failure criteria for brittle crack propagation in thermo-elastic solids. Comput. Methods Appl. Mech. Engrg. 294 449-485
- Miehe, C., Schänzel, L.-M., 2014. Phase field modeling of fracture in rubbery polymers.
 Part I: Finite elasticity coupled with brittle failure. J. Mech. Phys. Solids 65, 93–113.
- Miehe, C., Welschinger, F., Hofacker, M., 2010b. Thermodynamically consistent phase-field models of fracture: Variational principles and multi-field FE implementations. Internat. J. Numer. Methods Engrg. 83 (10), 1273–1311.
- Molnár, G., Gravouil, A., 2017. 2D and 3D abaqus implementation of a robust staggered phase-field solution for modeling brittle fracture. Finite Elem. Anal. Des. 130, 27–38.
- Mulderrig, J., Talamini, B., Bouklas, N., 2023. A statistical mechanics framework for polymer chain scission, based on the concepts of distorted bond potential and asymptotic matching. J. Mech. Phys. Solids 174, 105244.
- Peerlings, R.H.J., de Borst, R., Brekelmans, W.A.M., de Vree, J.H.P., 1996. Gradient enhanced damage for quasi-brittle materials. Internat. J. Numer. Methods Engrg. 39 (19), 3391–3403.
- Peerlings, R.H.J., de Borst, R., Brekelmans, W.A.M., Geers, M.G.D, 1998. Gradient-enhanced damage modelling of concrete fracture. Mech. Cohes. Frict. Mater. Int. J. Exp. Model Comput. Mater. Struct. 3 (4), 323–342.
- Pijaudier-Cabot, G., Bažant, Z.P., 1987. Nonlocal damage theory. J. Eng. Mech. 113 (10), 1512–1533.
- Press, W.H., Teukolsky, S.A., Vetterling, W.T., Flannery, B.P., 2007. Numerical Recipes 3rd Edition: The Art of Scientific Computing. Cambridge University Press.
- Raina, A., Miehe, C., 2016. A phase-field model for fracture in biological tissues. Biomech. Model. Mechanobiol. 15 (3), 479–496.
- Reinoso, J., Paggi, M., Linder, C., 2017. Phase field modeling of brittle fracture for enhanced assumed strain shells at large deformations: formulation and finite element implementation. Comput. Mech. 59 (6), 981–1001.
- Russ, J., Slesarenko, V., Rudykh, S., Waisman, H., 2020. Rupture of 3D-printed hyperelastic composites: Experiments and phase field fracture modeling. J. Mech. Phys. Solids 140, 103941.
- Slootman, J., Yeh, C.J., Millereau, P., Comtet, J., Creton, C., 2022. A molecular interpretation of the toughness of multiple network elastomers at high temperature. Proc. Natl. Acad. Sci. 119 (13), e2116127119.
- Talamini, B., Mao, Y., Anand, L., 2018. Progressive damage and rupture in polymers. J. Mech. Phys. Solids 111, 434–457.
- Vernerey, F.J., 2018. Transient response of nonlinear polymer networks: A kinetic theory. J. Mech. Phys. Solids 115, 230–247.
- Vernerey, F.J., Brighenti, R., Long, R., Shen, T., 2018. Statistical damage mechanics of polymer networks. Macromolecules 51 (17), 6609–6622.
- Wu, J., McAuliffe, C., Waisman, H., Deodatis, G., 2016. Stochastic analysis of polymer composites rupture at large deformations modeled by a phase field method. Comput. Methods Appl. Mech. Engrg. 312, 596–634.
- Yu, W.-W., Xu, W.-Z., Xia, J.-H., Wei, Y.-C., Liao, S., Luo, M.-C., 2020. Toughening natural rubber by the innate sacrificial network. Polymer 194, 122419.
- Zhong, M., Wang, R., Kawamoto, K., Olsen, B.D., Johnson, J.A., 2016. Quantifying the impact of molecular defects on polymer network elasticity. Science 353 (6305), 1264–1268.